Available online at www.sciencedirect.com

ScienceDirect

Geochimica et Cosmochimica Acta 257 (2019) 110–130

Geochimica et Cosmochimica Acta

www.elsevier.com/locate/gca

Enrichment mechanisms of antimony and arsenic in marine ferromanganese oxides: Insights from the structural similarity

Hai-Bo Qin [a,b,c,*], Soichiro Uesugi [a], Shitong Yang [a], Masato Tanaka [a], Teruhiko Kashiwabara [d], Takaaki Itai [a], Akira Usui [e], Yoshio Takahashi [a,*]

[a] *Department of Earth and Planetary Science, Graduate School of Science, The University of Tokyo, Hongo 7-3-1, Bunkyo-ku, Tokyo 113-0033, Japan*

[b] *State Key Laboratory of Environmental Geochemistry, Institute of Geochemistry, Chinese Academy of Sciences, Guiyang 550081, China*

[c] *CAS Center for Excellence in Quaternary Science and Global Change, Xi'an 710061, China*

[d] *Next-generation Technology for Ocean Resources Exploration Unit/Research and Development (R & D) Center for Submarine Resources, Japan Agency for Marine-Earth Science and Technology (JAMSTEC), 2-15 Natsushimacho, Yokosuka, Kanagawa 237-0061, Japan*

[e] *Geology Department, Kochi University, 2-5-1 Akebono, Kochi, Japan*

Received 9 November 2018; accepted in revised form 18 April 2019; available online 27 April 2019

Abstract

Marine ferromanganese crusts and nodules as potential mineral deposits have received increasing attention. However, much less knowledge is available concerning the incorporation and enrichment mechanisms for antimony (Sb) and arsenic (As) in marine ferromanganese oxides. In this study, the surface complexations of Sb(V) and As(V) on synthetic ferrihydrite and Mn oxides (δ-MnO_2 and birnessite) were investigated by a combination of adsorption experiments, extended X-ray absorption fine structure (EXAFS) analyses, and quantum chemical calculations. The speciation, distribution, and local structure of Sb and As in different types of natural marine ferromanganese oxides were determined by X-ray absorption near edge structure (XANES) and EXAFS analyses to reveal the enrichment mechanisms for the two elements in ferromanganese oxides at the molecular level. To the best of our knowledge, the Sb EXAFS analyses for different types of marine ferromanganese oxides are herein reported for the first time. Results showed that Sb(V) is preferentially adsorbed on Mn oxides through energetically favorable bidentate–mononuclear complexation because of the structural similarity between the octahedron $Sb^{V}(OH)_6^-$ and MnO_6 unit, although bidentate–binuclear (corner-sharing) and bidentate–mononuclear (edge-sharing) complexes can be formed on ferrihydrite and Mn oxides for the adsorption of Sb(V). By contrast, tetrahedral $As^{V}O_4^{3-}$ is mostly adsorbed on ferrihydrite and Mn oxides with the formation of bidentate–binuclear complexes. In natural marine ferromanganese oxides, Sb and As can be retained by Fe and Mn (oxyhydr)oxide components, and the disparate distribution of the two elements to Mn oxides may largely depend on the Mn/Fe ratio and constituent minerals. The larger enrichment factor of Sb than that of As in marine ferromanganese oxides may result from their preferential attachment modes onto the Fe and Mn phases and different inhibition effects from coexisting anions in seawater. Compared with As, a part of Sb may be strongly associated with the lateral sites in Mn oxides via the formation of bidentate edge-sharing complexes, with which anions such as sulfate in seawater do not significantly compete. The findings from this study provide the molecular-scale insights into the

* Corresponding authors at: Department of Earth and Planetary Science, Graduate School of Science, The University of Tokyo, Hongo 7-3-1, Bunkyo-ku, Tokyo 113-0033, Japan and State Key Laboratory of Environmental Geochemistry, Institute of Geochemistry, Chinese Academy of Sciences, Guiyang 550081, China (H.-B. Qin).

E-mail addresses: qinhaibo@vip.gyig.ac.cn (H.-B. Qin), ytakaha@eps.s.u-tokyo.ac.jp (Y. Takahashi).

https://doi.org/10.1016/j.gca.2019.04.018

enrichment processes and mechanisms of Sb and As in marine ferromanganese oxides. Our study also helps elucidate the incorporation mechanisms and geochemical behaviors of other oxyanions in marine and surface environments.

Keywords: Marine ferromanganese oxides; Antimony (Sb); Arsenic (As); EXAFS; Surface complex; Enrichment mechanisms

1. INTRODUCTION

Ferromanganese oxides, aggregates of iron (oxyhydr)oxides and manganese oxides, are mainly present in the forms of nodules and crusts in various environments, such as soils, sedimentary rocks, lakes, caves, and deep oceans (Manceau et al., 2003; Takahashi et al., 2007; Frierdich and Catalano, 2012; Liu et al., 2017). Marine ferromanganese oxides can be generally classified into hydrogenetic (HG) nodules and crusts, diagenetic (DG) and hydrothermal (HT) deposits, on the basis of the Mn/Fe ratios, growth rates, and constituent Mn minerals (Glasby, 2006; Takahashi et al., 2007; Bau et al., 2014). Marine ferromanganese oxides are generally considered to be a potential mineral deposit, which may be an additional supplement to land-based resources, because they can act as the efficient scavengers for many rare and critical elements, such as tellurium (Te), cobalt (Co), molybdenum (Mo), and tungsten (W) from seawater (Hein et al., 2003, 2013; Kashiwabara et al., 2011, 2014; Takahashi et al., 2015). For example, Te can be extremely enriched in marine ferromanganese oxides with an enrichment factor of $\sim 10^9$ times relative to seawater (Hein et al., 2003; Kashiwabara et al., 2014; Qin et al., 2017a). Over the past decades, deep-ocean ferromanganese crusts and nodules have aroused increasing interest as potential mineral resources. However, much less knowledge is available concerning the incorporation and enrichment mechanisms of trace elements in marine ferromanganese oxides.

Antimony (Sb) is a critical metalloid, which has large industrial applications, such as heat stabilizers in plastics, as well as additives in the production of brake linings, pigments, microelectronics, and semiconductors (Filella et al., 2002). Arsenic (As), belonging to the same group 15 of the periodic table as Sb, is also widely applied to the production of pesticides, alloys, and semiconductors (Mandal and Suzuki, 2002). Antimony can be found in nature as a sulfide mineral (stibnite) in the Sb deposits, but its supply risk is high, whereas As is generally extracted from the by-products of gold and copper mines (USGS, 2012). Nonetheless, with high consumer demand and mining activities, numerous emissions have resulted in elevated Sb and As concentrations in water, soils, and plants, posing a serious health risk because the two elements are highly toxic to human beings (Filella et al., 2002; Mandal and Suzuki, 2002). Additionally, high contents of Sb and As have been also observed in deep-ocean ferromanganese oxides (e.g., Usui and Someya, 1997; Hein et al., 2003, 2013; Marcus et al., 2004). For example, the average abundances of Sb and As in ferromanganese crusts and nodules from the North Pacific are 41 and 389 mg kg^{-1}, respectively (Hein et al., 2013). However, in contrast to considerable researches with respect to the distribution, mobility, transformation, bioavailability, and toxicity of the two elements in surface environment (e.g., Mitsunobu et al., 2006; Scheinost et al., 2006), few studies have focused on those for Sb and As in the marine environment.

Antimony and As can exist in several oxidation states (−III, 0, III, and V), and each species shows different geochemical behaviors (Filella et al., 2002; Mandal and Suzuki, 2002). In soil environments, Sb(V) is the stable species over a wide redox range (Mitsunobu et al., 2006; Scheinost et al., 2006), whereas As can be present as a mixture of As(III) and As(V) species (Mitsunobu et al., 2006). In seawater, Sb and As are predominantly present as the pentavalent oxyanions, $Sb(OH)_6^-$ and AsO_4^{3-}, respectively (Filella et al., 2002). Nevertheless, the speciation of the two elements in marine ferromanganese oxides, which governs their geochemical behaviors and fates, is largely unknown due to their low concentration and challenging analysis method.

Sequential extraction procedures have been extensively employed to determine the speciation and host phase of target elements including Sb and As, but this approach may lead to controversial conclusions owing to possible readsorption and incomplete selectivity for some elements during extraction process (Takahashi et al., 2007; Qin et al., 2012, 2013, 2017b). Alternatively, the direct X-ray absorption fine structure (XAFS) approach, which consists of X-ray absorption near edge structure (XANES) and extended X-ray absorption fine structure (EXAFS), has been widely utilized to identify the speciation and local structure of metal(loid)s in solid samples nondestructively (e.g., Mitsunobu et al., 2006; Qin et al., 2012, 2017a, b; Li et al., 2018).

By EXAFS spectroscopy, Marcus et al. (2004) indicated that As is strictly associated with ferrihydrite and is mostly pentavalent in a fast-growing diagenetic ferromanganese nodule from the Baltic Sea. Similarly, Manceau et al. (2007) found that ferrihydrite is the main host phase of As in ferromanganese coatings on quartz grains from waterwork sand-filters. Nonetheless, Liu et al. (2017) recently observed that As can be also retained by Mn oxides in ferromanganese duricrust via the formation of bidentate-binuclear complexes, and they highlighted the mineralogical constraints on the distribution and partition of As in natural samples. In contrast to the widespread interest on As, very few EXAFS study has been attempted for Sb in natural ferromanganese oxides. Kashiwabara et al. (2008) firstly determined the oxidation states of Sb in two hydrogenetic ferromanganese samples by XANES analysis, but the host phase of Sb is not clearly identified in this study. In addition, the distributions of trace elements and rare earths and yttrium (REY) are significantly distinct in hydroge-

netic, diagenetic, and hydrothermal ferromanganese samples (Koschinsky and Halbach, 1995; Takahashi et al., 2007; Bau et al., 2014). For example, the host phase of lead would be transferred from the Mn-Fe phase to the apatite during the phosphatization of marine ferromanganese crusts (Koschinsky and Halbach, 1995). Hence, determining the distribution, speciation, and molecular-scale structural information of Sb and As in different types of marine ferromanganese oxides is necessary to better understand geochemical behaviors and the partitioning of the two elements in marine environment.

Moreover, the enrichment factor of Sb is remarkably higher than that of As in marine ferromanganese oxides relative to seawater (e.g., Hein et al., 2003, Takahashi et al., 2015), but this discrepancy is not well understood yet. For the element dissolved in seawater as anion, the enrichment degree in hydrogenetic ferromanganese oxides generally depends on its proton dissociation constant (pK_a), as summarized by Takahashi et al. (2015). Nevertheless, this assertion is not enough to explain the different enrichment factors between Sb and As in marine ferromanganese oxides, since the two elements have similar pK_a values (Kashiwabara et al., 2008). In marine ferromanganese oxides, ferrihydrite and vernadite (corresponding to synthetic δ-MnO_2) have been demonstrated to be the dominant Fe and Mn phases by EXAFS and X-ray diffraction (XRD) analyses, although other Fe and Mn phases may be also present (e. g., Takahashi et al., 2007; Marcus et al., 2004, 2015; Yang et al., 2019). Interestingly, significantly different adsorption behaviors have been found for Sb and As on metal (Fe and Mn) oxides by numerous laboratory studies (e.g., Manceau, 1995; Foster et al., 2003; Mitsunobu et al., 2006, 2010; Zhang et al., 2014). Thus, it is essential to systematically compare the uptake mechanisms and controlling factors for the two elements in seawater by Fe and Mn oxides for a better understanding of the larger enrichment factor of Sb compared with As in marine ferromanganese samples.

In the present study, we investigated the surface complexes of Sb(V) and As(V) adsorbed on synthetic ferrihydrite and Mn oxides at the molecular scale by a combination of adsorption experiments, quantum chemical calculations, and EXAFS analyses. Meanwhile, we determined and compared the distribution, speciation, and local environment of Sb and As in different types of marine ferromanganese oxides by XAFS technique. The objectives of this work are (i) to reveal the nature of surface complexes for Sb(V) and As(V) adsorbed on Fe and Mn oxides, (ii) to clarify mineralogical constraints and enrichment mechanisms for Sb and As in marine ferromanganese oxides at the molecular level, and (iii) to provide insights into the geochemical processes and fates of trace elements in marine and surface environments.

2. EXPERIMENTAL

2.1. Samples and materials

Four hydrogenetic, four diagenetic, and one hydrothermal ferromanganese oxide samples collected during several research cruises in the Central to Northwest Pacific Ocean and the Central Indian Ocean were selected for this study, the details are summarized in Table 1 (Takahashi et al., 2007). These samples were air dried and crushed into powder using an agate mortar. The powder samples were sealed into polyethylene bags and then stored in a vacuum sealed jar for chemical analysis and XAFS measurement to avoid possible mineralogical transformation under air condition. In this study, we checked the mineralogical characterizations for several selected hydrogenetic (AD14, CD25) and diagenetic (F243-1) samples by XRD analysis, and the XRD patterns obtained herein (Fig. S1) were identical to those reported previously by Takahashi et al. (2007). In the hydrogenetic ferromanganese samples, Fe was present as predominant ferrihydrite (84%), along with 11% hematite (or feroxyhite) and 5% goethite, while δ-MnO_2 is the main Mn phase by EXAFS analyses (Yang et al., 2019). The total concentrations of Sb and As in samples were determined by ICP-MS (Agilent Technologies, Agilent 7700) after acid digestion, as described previously by Takahashi et al. (2007). Two hydrogenetic (D535 and D886) and two diagenetic (F243-1 and B6) samples were selected to collect Sb and As K-edge XAFS spectra.

Two-line ferrihydrite, δ-MnO_2, and birnessite were prepared following the proposed procedures by Schwertmann and Cornell (2000), Foster et al. (2003), and Villalobos et al. (2003), respectively. In brief, 2-line ferrihydrite was synthesized by adjusting a solution containing 36 mM Fe $(NO_3)_3{\cdot}9H_2O$ to pH 8.0 through the dropwise addition of 4.0 M NaOH solution, then the obtained suspension was aged overnight. δ-MnO_2 was prepared by the rapid oxidation of a 30 mM $MnCl_2$ solution with an equal volume of a 20 mM $KMnO_4$ solution at pH 10. Birnessite was synthesized through the acid reduction of a boiling $KMnO_4$ solution using concentrated HCl. These solid phases were recovered by filtering, washing, and freeze-drying, and then were identified by XRD measurement.

2.2. Adsorption experiments

Two series of adsorption experiments were performed using 50 mg of absorbents (2-line ferrihydrite or δ-MnO_2) and 20 mL of Sb or As solution in 25 mL polystyrene vessels under the following experimental conditions: In the first series, adsorption isotherms were obtained at different initial concentrations of Sb(V) or As(V) at pH 8.0 with an ionic strength of 0.70 M ($NaNO_3$), as previously described for Mo and W (Kashiwabara et al., 2011, 2013). By comparison, the ionic strength was adjusted by artificial seawater (ASW) instead of $NaNO_3$ in the second series experiments to better simulate Sb and As behaviors in marine environment. The stock solutions of 60 mM Sb(V) and As(V) were prepared by dissolving $K[Sb(OH)_6]$ and NaH_2AsO_4 in Milli-Q water, respectively. The ASW consisted of 440 mM NaCl, 50 mM $MgCl_2{\cdot}2H_2O$, 27 mM Na_2SO_4, 9.6 mM $CaCl_2{\cdot}2H_2O$, and 2.2 mM $NaHCO_3$ (Tokunaga and Takahashi, 2017). The pH was maintained by adding a small amount of 0.10 M NaOH or HNO_3. The vessels were shaken in a shaking bath at room temperature. After 24 h, the samples were filtered using disposable syringes

Table 1
List of the marine ferromanganese oxide samples in this study.

Sample	Sampling site			Cruise name	Type
	Latitude	Longitude	Depth (m)		
AD14	14°11.8′N	167°24.4′E	1617	Hakurei-maru 96S	HG
D535	13°00.6′S	159°17.6′W	5222	Hakurei-maru GH83-3	HG
CD25	16°26.0′N	169°32.3′W	2320	Farnella FN-86-HW	HG
D886	27°06.0′N	145°12.5′E	1880	Hakurei-maru GH86-3	HG
FG352	03°15.8′N	169°41.1′W	5370	Hakurei-maru GH81-4	DG
B6	30°17.8′N	172°10.5′W	5350	Hakurei-maru GH80-1	DG
G181	07°01.4′N	171°59.7′W	5660	Hakurei-maru GH76-1	DG
F243-1	07°40.2′N	172°56.3′W	5907	Hakurei-maru GH80-1	DG
D12-X2	31°58.0′N	139°04.2′E	1590	Moana Wave MW9503	HT

HG: hydrogenetic; DG: diagenetic; HT: hydrothermal.

(0.2 μm). The filtrates were adequately diluted to determine the concentrations of Sb or As by ICP-MS. All the experiments were repeated three times to evaluate precision.

In addition, adsorbed samples with different loading levels ([Sb(As)/Fe(Mn)] molar ratios = 0.001, 0.005, and 0.01) were prepared by adding appropriate amounts of stock solution of Sb(V) and As(V) to 2-line ferrihydrite, δ-MnO_2, and birnessite under similar experimental conditions. After equilibration in a shaking water bath at room temperature for 24 h, the suspensions were filtered using a membrane filter (0.2 μm). The solid phases were rinsed with Milli-Q water at least three times and then packed into polyethylene bags for XAFS measurements.

2.3. XAFS measurements and data analyses

Antimony K-edge XAFS spectra were obtained at the beamline BL01B1 at SPring-8 (Hyogo, Japan) with a Si (311) double-crystal monochromator and two mirrors, whereas As K-edge XAFS spectra were measured at the beamline BL12C at the Photon Factory, KEK (Tsukuba, Japan) or BL01B1 at SPring-8 with a Si(111) double-crystal monochromator. The adsorbed and natural samples were placed at an angle of 45° from the incident beam and recorded in fluorescence mode using a 19-element Ge solid-state detector, whereas those for the standard materials were measured in transmission mode. The energies of Sb and As were calibrated using the peak of K[$Sb(OH_6)$] at 30.492 keV and KH_2AsO_4 at 11.862 keV, respectively. The measurements were conducted at room temperature under ambient air conditions. Multiple scans were performed to improve the signal-to-noise ratio. No radiation damage was detected during data acquisition.

The EXAFS data were analyzed using REX2000 (Rigaku Co. Ltd.) and FEFF 7.02 (Zabinsky et al., 1995). After extracting the EXAFS function from the raw spectra, the radial structural functions (RSFs) were obtained from the $k^3\chi(k)$ oscillation by Fourier transform (FT). The distinct RSF shells were then inversely transformed for spectral simulation by a curve-fitting method. In this calculation, the theoretical phase shifts and backscattering amplitude functions for Sb–O, Sb–Fe, and Sb–Mn were extracted from the structures of tripuhyite ($FeSb^VO_4$) (Berlepsch et al., 2003) and manganese diantimonate ($MnSb_2^VO_6$) (Reimers et al., 1989); while those for As–O, As–Fe, and As–Mn were extracted from the structures of scorodite ($FeAs^VO_4{\cdot}2H_2O$) (Kitahama et al., 1975) and manganese arsenate hydrate ($MnAs^VO_4{\cdot}H_2O$) (Aranda et al., 1991). Details of the EXAFS analysis were similar to those previously described (e.g., Mitsunobu et al. 2010; Yang et al., 2019). The quality of EXAFS simulation was evaluated by the goodness of fit parameter, R factor, expressed by the following equation:

$$R = \sum \{k^3 x_{obs}(k) - k^3 x_{cal}(k)\}^2 / \sum \{k^3 x_{obs}(k)\}^2 \quad (1)$$

where $\chi_{obs}(k)$ and $\chi_{cal}(k)$ are the experimental and calculated absorption coefficients at a given wavenumber (k), respectively.

The linear combination fittings (LCF) for the $k^3\chi(k)$ spectra of Sb and As in natural ferromanganese oxides samples were performed using reference materials (i.e., Sb(V) or As(V) adsorbed on ferrihydrite, δ-MnO_2, and birnessite) as end members within the range of 3–10 $Å^{-1}$ by the ATHENA software Package (Ravel and Newville, 2005).

2.4. Quantum chemical calculations

The density functional theory (DFT) calculations were performed for the surface complexes of Sb(V) and As(V) adsorbed on Fe (oxyhydr)oxide and Mn oxide. The geometrical parameter for the Fe (oxyhydr)oxide model was referred to goethite structure instead of amorphous ferrihydrite (Tanaka et al., 2014), and that for Mn oxide was referred to birnessite crystal structure (Tanaka et al., 2018). The geometry for each surface model of Fe/Mn (oxyhydr)oxides was fixed during geometry optimization. The charge of the entire system was neutral for each adsorption model system. The electronic states of Fe and Mn (oxyhydr)oxides systems were assumed to be high spin 11-et and 7-et states, respectively. The integral equation formalism of polarizable continuum model (IEFPCM) was employed to consider the solvent effects (Miertus et al., 1981).

The interaction energy (ΔE_{int}) between Sb(V) and the surface of Fe/Mn (oxyhydr)oxides was calculated for differ-

ent surface complex models, expressed by the following equation:

$$\Delta E_{int} = E_{A-B} - (E_A + E_B) \quad (2)$$

where E_A, E_B, and $E_{A\text{-}B}$ are the total energies of (i) the Fe/Mn (oxyhydr)oxides surface model, (ii) the Sb(V) oxyanion, and (iii) the whole structure of adsorbed complex with Fe/Mn (oxyhydr)oxides surface models, respectively. In practice, E_A and E_B were obtained by single point calculation with the partial geometries of Sb and Fe/Mn (oxyhydr)oxides surface in the optimized geometry of the whole structure of adsorbed complexes. The basis set superposition error (BSSE) in ΔE_{int} was corrected by the counterpoise method (Boys and Bernardi, 1970).

A hybrid functional, B3LYP (Lee et al., 1988; Becke, 1993; Stephens et al., 1994), was used with a 6-31+G* basis set for H and O atoms (Frisch et al., 1984) and a LANL2DZ basis set for Sb, As, Fe, and Mn atoms (Hay and Wadt, 1985; Wadt and Hay, 1985; Curtiss et al., 1995). All DFT calculations were performed using the Gaussian 09 program (Frisch et al., 2009).

3. RESULTS

3.1. Adsorption isotherms for Sb(V) and As(V) on synthetic ferrihydrite and δ-MnO_2

Fig. 1A and B show the adsorption isotherms for Sb(V) and As(V) on ferrihydrite and δ-MnO_2, respectively. All the adsorptions were described well by the Freundlich or the Langmuir equation, although significantly different adsorbed amounts were observed at higher Sb and As equilibrium concentrations among all systems. The adsorption of As(V) on δ-MnO_2 in the ASW system seemed to be saturated, whereas other systems did not reach the saturation state even up to the maximum initial concentrations (~600 μmol L^{-1}) for Sb(V) and As(V) under our experiment conditions.

The adsorption of As(V) on ferrihydrite was generally greater than those for Sb(V) particularly at lower concentrations (<160 μmol L^{-1}) either in the MQ water or the ASW system (Fig. 1A). On the contrary, Sb(V) was adsorbed on δ-MnO_2 in larger amounts than As(V) under artificial seawater conditions, in spite of a larger As(V) adsorption at lower concentrations (<60 μmol L^{-1}) in the MQ water system (Fig. 1B). Compared with the MQ water system, a significant reduction was found for As(V) adsorption on ferrihydrite and especially for δ-MnO_2 in the ASW system. In terms of Sb(V), an inhibition effect for its adsorption on ferrihydrite under artificial seawater conditions was clearly observed, but this influence was not found for δ-MnO_2.

3.2. EXAFS analyses for adsorbed samples

3.2.1. Sb K-edge EXAFS

The $k^3\chi(k)$ spectra of Sb K-edge EXAFS and their RSFs (phase shift not corrected) for Sb(V)-adsorbed samples at different loading levels are illustrated in Fig. 2A and B, respectively. The $k^3\chi(k)$ spectra of Sb(V)-adsorbed ferrihydrite (Fig. 2A(a), (b) and (c)) were significantly different from those of Sb(V)-adsorbed δ-MnO_2 (Fig. 2A(d), (e) and (f)) and birnessite (Fig. 2A(g)) around 6.5–8.5 $Å^{-1}$. In the RSFs, the first prominent peak was observed at R + ΔR = 1.5 Å for Sb(V)-adsorbed ferrihydrite and Mn oxide samples at different loading levels (Fig. 2B), which was simulated with the Sb–O shell at a similar distance (~1.97 Å) via a curve-fitting analysis (Table 2). The distant pronounced peaks in the RSFs of Sb(V)-adsorbed ferrihydrite were assigned to two Sb–Fe shells, and the fitted distance between Sb and Fe atoms was 3.08–3.11 Å and 3.53–3.57 Å for the Sb–Fe_1 and Sb–Fe_2 shells, respectively (Table 2). Similarly, in the case of Sb(V) on δ-MnO_2 and birnessite, the prominent peaks following the Sb–O shell were simulated by two Sb–Mn shells, whose interatomic distances were 2.99–3.02 Å ($R_{Sb\text{-}Mn1}$) and 3.44–3.48 Å ($R_{Sb\text{-}Mn2}$), respectively (Table 2). Furthermore, the imaginary parts of the FTs of adsorbed samples were also fitted well (Fig. S2), suggesting that the three-shell model is quite reasonable for Sb(V)-adsorbed ferrihydrite and Mn oxides.

3.2.2. As K-edge EXAFS

The $k^3\chi(k)$ spectra around 7–8 $Å^{-1}$ and 9–10 $Å^{-1}$ (Fig. 3A) and the RSFs around R + ΔR = 2.6–2.8 Å (Fig. 3B) for As(V)-adsorbed ferrihydrite were obviously distinct from those for As(V)-adsorbed Mn oxides. Unlike Sb(V)-adsorbed samples, the As–O–O path was included during the curve-fitting analysis for As(V)-adsorbed samples, considering that the AsO_4 multiple scattering may produce signals in the weak second shell. As a result, the first peaks in the RSFs were composed of approximately four O atoms at a distance of 1.69–1.70 Å from the central As atom, while the distant peaks were simulated by the As–Fe shell at ~3.27 Å and the As–Mn shell at ~3.18 Å for ferrihydrite and Mn oxides at different loading levels (Table 3).

3.3. DFT calculations

Fig. 4 shows the optimized geometries of different surface complex models for Sb adsorbed on Fe (oxyhydr)oxide and Mn oxide. The predicted Sb–O distance was 1.98 Å for all the surface complex modes. The interatomic distances between Sb and metal (Fe or Mn) atoms in the bidentate–mononuclear (edge-sharing, ^2E) and bidentate–binuclear (corner-sharing, ^2C) complexes for Fe (oxyhydr)oxide were 3.19 Å and 3.57 Å, respectively (Fig. 4a and c); whereas those for Mn oxide were 3.06 Å and 3.54 Å, respectively (Fig. 4b and d).

Despite a lower ΔE_{int} value for the bidentate–binuclear than that of the bidentate–mononuclear complex (Fig. 4a and c), the difference of their ΔE_{int} value was relatively small (~3.9 kcal mol^{-1}), possibly implying the similar contribution from both surface complexes to Sb(V) adsorption on Fe (oxyhydr)oxide. By contrast, considerably different ΔE_{int} values were observed for the two surface complexes (~37.3 kcal mol^{-1}) on Mn oxide (Fig. 4b and d), which clearly indicates that the bidentate-mononuclear complex

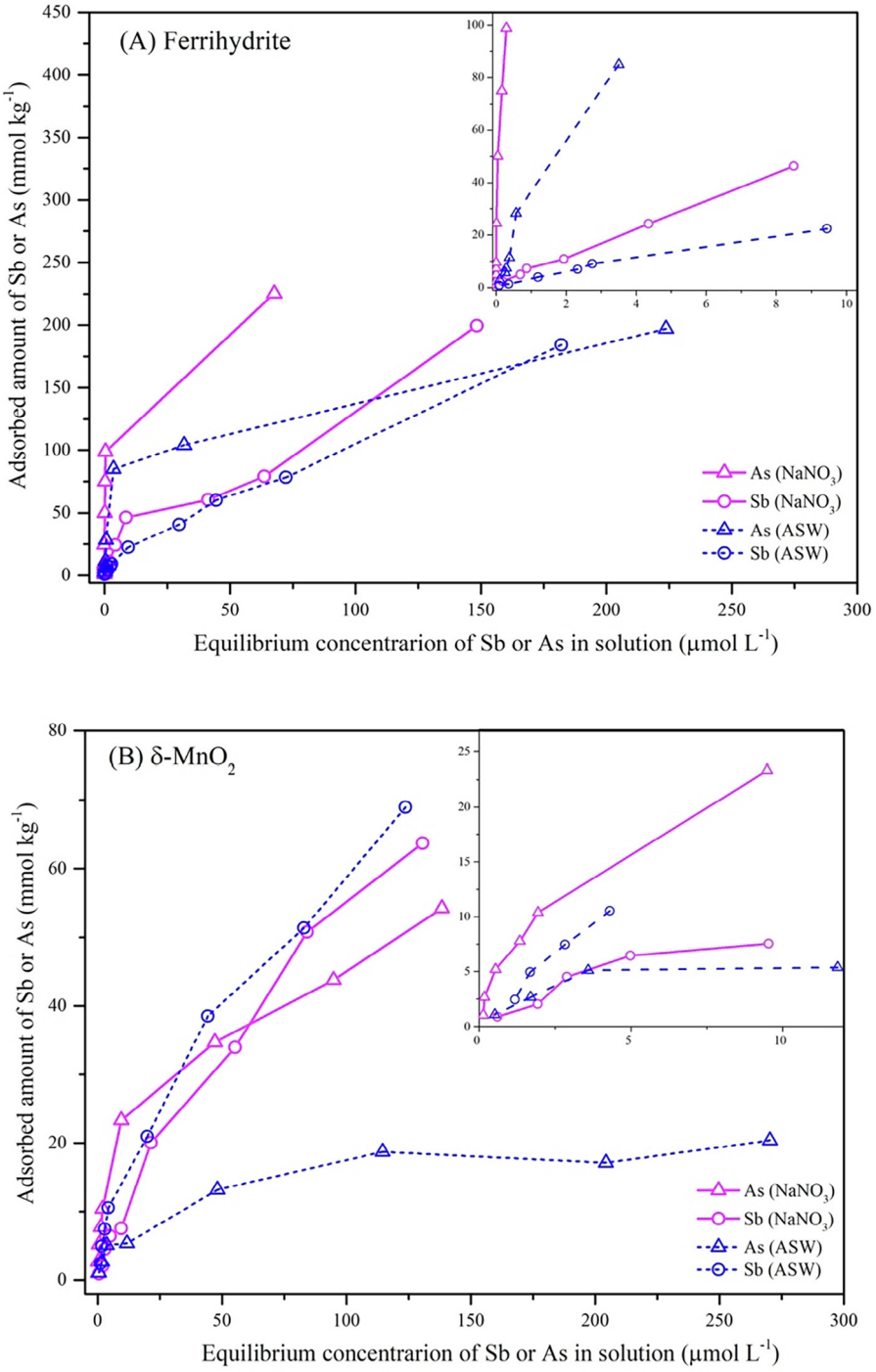

Fig. 1. Adsorption isotherms for Sb(V) or As(V) on ferrihydrite (A) and δ-MnO_2 (B) in the MQ water and ASW system.

is energetically favorable relative to the bidentate-binuclear complex for the adsorption of Sb(V) on Mn oxide.

3.4. Analyses of natural marine ferromanganese oxides

3.4.1. Concentrations of Sb and As

The concentration of Sb and As in natural marine ferromanganese samples were 22.7–44.5 and 16.8–194 mg kg^{-1}, respectively (Table 4). The values range within the Sb and As levels in ferromanganese crusts and nodules from different areas of the global ocean (e.g., Usui and Someya, 1997; Hein et al., 2012, 2013). For different genetic types of ferromanganese oxides, Sb content increased from HG (25.7 ± 2.9 mg kg^{-1}), DG (34.6 ± 7.5 mg kg^{-1}), and HT (44.5 mg kg^{-1}) deposits, whereas a significant decrease was found for As concentration in HG (153 ± 32.5 mg kg^{-1}), DG (90.3 ± 53.2 mg kg^{-1}), and HT (16.8 mg kg^{-1}) samples. Moreover, the enrichment factor

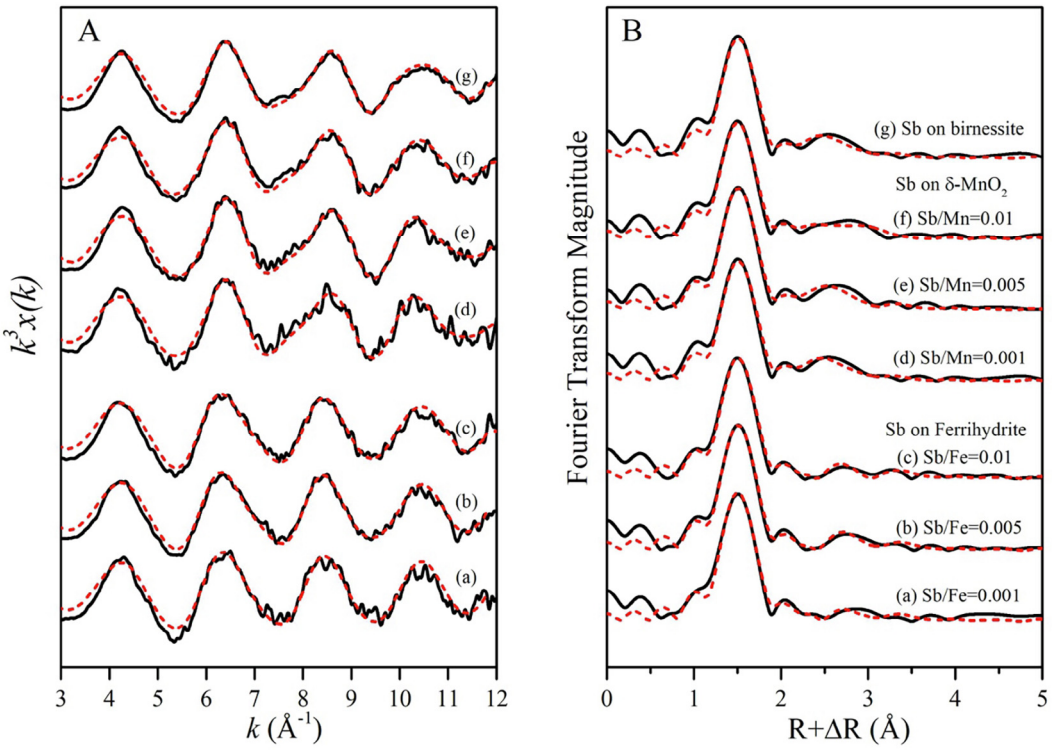

Fig. 2. Sb K-edge EXAFS spectra for adsorbed samples: (A) k^3-weighted $x(k)$ spectra, and (B) their RSFs (phase shift not corrected). Solid lines are spectra obtained by experiments, and red dash lines are calculated spectra by a curve-fitting analysis. (For interpretation of the references to colour in this figure legend, the reader is referred to the web version of this article.)

Table 2
Structural parameters of Sb(V) adsorbed on ferrihydrite, δ-MnO_2, and birnessite at different loading levels obtained by a curve-fitting analysis of EXAFS spectra.

Sample	Shell	CN	R (Å)	ΔE_0 (eV)	σ^2 (Å^2)	R factor (%)
Sb on ferrihydrite	Sb-O	6.5(0.5)	1.97(0.01)	6.47	0.003	3.23
(Sb/Fe = 0.001)	Sb-Fe_1	0.4(0.6)	3.08(0.05)		0.004[a]	
	Sb-Fe_2	1.1(0.9)	3.53(0.05)		0.004[a]	
Sb on ferrihydrite	Sb-O	6.4(0.5)	1.97(0.01)	6.89	0.003	1.74
(Sb/Fe = 0.005)	Sb-Fe_1	0.8(0.6)	3.11(0.04)		0.004[a]	
	Sb-Fe_2	1.1(0.9)	3.56(0.05)		0.004[a]	
Sb on ferrihydrite	Sb-O	6.3(0.5)	1.97(0.01)	6.71	0.003	1.77
(Sb/Fe = 0.01)	Sb-Fe_1	0.7(0.5)	3.09(0.05)		0.004[a]	
	Sb-Fe_2	1.0(0.9)	3.57(0.05)		0.004[a]	
Sb on δ-MnO_2	Sb-O	6.4(0.5)	1.98(0.01)	6.73	0.003	3.09
(Sb/Mn = 0.001)	Sb-Mn_1	1.6(0.5)	2.99(0.02)		0.004[a]	
	Sb-Mn_2	0.7(0.7)	3.48(0.07)		0.004[a]	
Sb on δ-MnO_2	Sb-O	6.3(0.5)	1.97(0.01)	6.54	0.003	1.97
(Sb/Mn = 0.005)	Sb-Mn_1	1.6(0.5)	3.00(0.02)		0.004[a]	
	Sb-Mn_2	0.9(0.7)	3.48(0.06)		0.004[a]	
Sb on δ-MnO_2	Sb-O	6.1(0.5)	1.97(0.01)	5.73	0.003	2.52
(Sb/Mn = 0.01)	Sb-Mn_1	1.0(0.5)	3.00(0.03)		0.004[a]	
	Sb-Mn_2	0.9(0.7)	3.45(0.04)		0.004[a]	
Sb on birnessite	Sb-O	6.4(0.5)	1.97(0.01)	6.62	0.004	1.53
(Sb/Mn = 0.01)	Sb-Mn_1	1.0(0.5)	3.02(0.03)		0.004[a]	
	Sb-Mn_2	1.5(0.7)	3.44(0.03)		0.004[a]	

The estimated errors (standard deviations) are given in parentheses.
CN, coordination number; R, interatomic distance; ΔE_0, threshfold E_0 shift; and σ^2, Debye-Waller factor.
[a] Constrained to a same value in the fitting process.

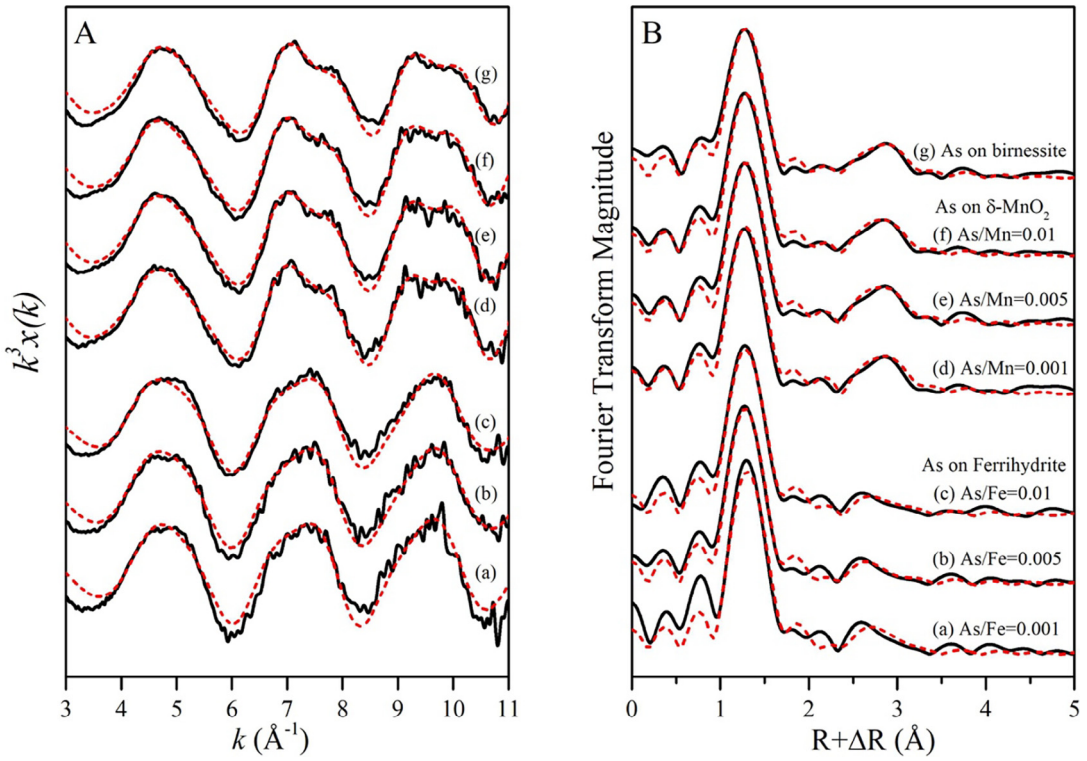

Fig. 3. As K-edge EXAFS spectra for adsorbed samples: (A) k^3-weighted $x(k)$ spectra, and (B) their RSFs (phase shift not corrected). Solid lines are spectra obtained by experiments, and red dash lines are calculated spectra by a curve-fitting analysis. (For interpretation of the references to colour in this figure legend, the reader is referred to the web version of this article.)

of Sb and As was calculated as the ratio of the two elemental concentrations in the ferromanganese oxides relative to the average abundance in seawater (0.18 and 1.7 μg L^{-1} for Sb and As, respectively; Filella et al., 2002). As a result, the enrichment factor of Sb (1.3×10^5–2.5×10^5) was remarkably higher than that of As (9.9×10^3–1.1×10^5) in marine ferromanganese oxides. The enrichment factor of Sb showed an increasing trend in the order of HG < DG < HT samples, whereas that of As presented an opposite trend in the three types of ferromanganese oxides.

Fig. 5 shows that Sb was positively correlated with Mn ($r = 0.640$, $p > 0.05$), but As was positively correlated with Fe ($r = 0.724$, $p < 0.01$) in marine ferromanganese samples. This result is consistent with the interelement correlation analyses for Sb and As in abyssal Pacific ferromanganese nodules (Li, 1982). Meanwhile, the Mn/Fe ratio against Sb and As, as well as the Sb/As ratio are also plotted in Fig. 6. With increased Mn/Fe ratio, Sb concentration generally increased (Fig. 6A), whereas As content in ferromanganese oxides obviously decreased (Fig. 6B). A significantly positive correlation ($r = 0.769$, $p < 0.01$) was found between Sb/As and Mn/Fe ratios for marine ferromanganese samples (Fig. 6C).

3.4.2. Sb and As K-edge XANES spectra for selected ferromanganese samples

The peak energies of Sb XANES spectra for ferromanganese oxides and adsorbed samples (ferrihydrite and δ-MnO_2) were essentially identical to that of the Sb(V) solution (Fig. 7A), which suggests that Sb is present exclusively as Sb(V) in the marine ferromanganese samples examined in this study, and no reduction occurs upon Sb (V) adsorption on ferrihydrite and δ-MnO_2. In terms of the As XANES spectra, the peak positions of all the examined natural and adsorbed samples were highly similar to that of the As(V) solution (Fig. 7B), indicating that As is pentavalent in marine ferromanganese oxides. However, determining the proportions of Sb or As associated with Fe and Mn oxides via LCF analysis is difficult because of their similar XANES spectra.

3.4.3. Sb EXAFS spectra for selected ferromanganese samples

Fig. 8A shows the $k^3\chi(k)$ spectra of Sb for a selection of hydrogenetic (D535 and D886) and diagenetic (B6 and F243-1) ferromanganese oxides and reference materials. The $k^3\chi(k)$ spectra for samples D535, D886, and B6 resembled each other and were basically similar to that of Sb(V)-adsorbed ferrihydrite, which can be reconstructed by combining 71%–86% Sb(V)-adsorbed ferrihydrite and less amounts of Sb(V)-adsorbed δ-MnO_2 (14%–29%) by the LCF analysis (Table 5). By contrast, the EXAFS spectrum for F243-1 was significantly different from those of other marine ferromanganese samples, which was reproduced by large amounts of Sb(V)-adsorbed birnessite (54%) aside from Sb(V)-adsorbed ferrihydrite (46%).

In spite of the relatively poor quality for Sb EXAFS spectra of natural ferromanganese samples, the structural

Table 3
Structural parameters of As(V) adsorbed on ferrihydrite, δ-MnO_2, and birnessite at different loading levels obtained by a curve-fitting analysis of EXAFS spectra.

Sample	Shell	CN	R (Å)	ΔE_0 (eV)	σ^2 (Å^2)	R factor (%)
As on ferrihydrite	As-O	4.1(0.2)	1.70(0.01)	7.05	0.002	3.23
(As/Fe = 0.001)	As-O-O	12[a]	3.08		0.002	
	As-Fe	1.6(0.7)	3.27(0.03)		0.006	
As on ferrihydrite	As-O	4.6(0.2)	1.69(0.01)	6.98	0.002	1.12
(As/Fe = 0.005)	As-O-O	12[a]	3.08		0.002	
	As-Fe	1.2(0.6)	3.27(0.04)		0.006	
As on ferrihydrite	As-O	4.5(0.2)	1.69(0.01)	6.45	0.002	1.15
(As/Fe = 0.01)	As-O-O	12[a]	3.08		0.002	
	As-Fe	1.2(0.6)	3.27(0.04)		0.006	
As on δ-MnO_2	As-O	4.5(0.2)	1.70(0.01)	6.78	0.002	1.78
(As/Mn = 0.001)	As-O-O	12[a]	3.09		0.002	
	As-Mn	1.8(0.4)	3.18(0.02)		0.004	
As on δ-MnO_2	As-O	4.4(0.2)	1.70(0.01)	6.74	0.002	1.91
(As/Mn = 0.005)	As-O-O	12[a]	3.09		0.002	
	As-Mn	1.8(0.4)	3.18(0.01)		0.004	
As on δ-MnO_2	As-O	4.4(0.2)	1.70(0.01)	6.60	0.002	1.66
(As/Mn = 0.01)	As-O-O	12[a]	3.09		0.002	
	As-Mn	1.8(0.4)	3.18(0.01)		0.004	
As on birnessite	As-O	4.2(0.2)	1.70(0.01)	8.91	0.002	2.03
(As/Mn = 0.01)	As-O-O	12[a]	3.09		0.002	
	As-Mn_2	1.8(0.4)	3.17(0.02)		0.004	

The estimated errors (standard deviations) are given in parentheses.
[a] Fixed to be 12 for $CN_{As\text{-}O\text{-}O}$ due to multiple scatting of O-O pairs in the AsO_4 tetrahedron. $\sigma^2_{As\text{-}O\text{-}O}$ is constrained to be equal to $\sigma^2_{As\text{-}O}$ during the spectral fit procedures.

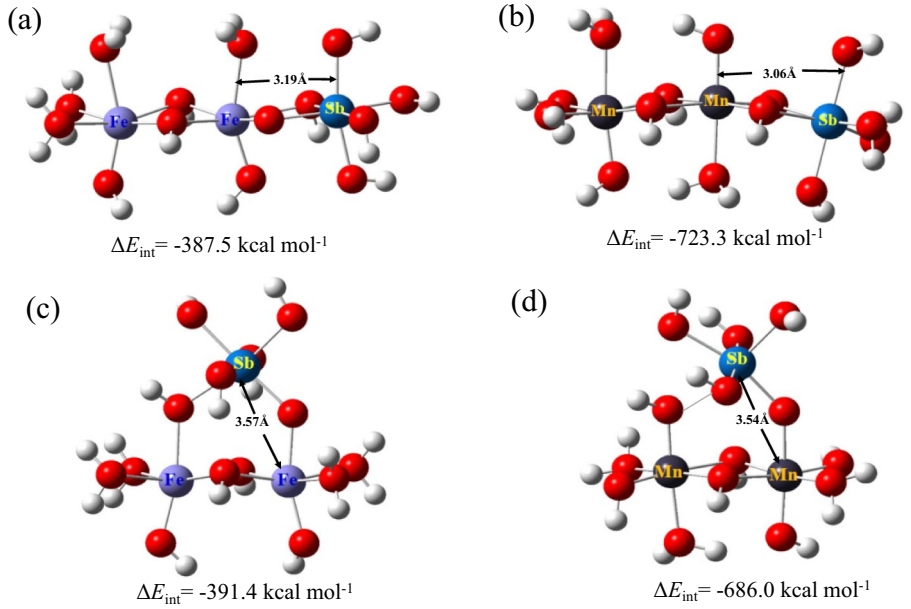

ΔE_{int}= -387.5 kcal mol^{-1} ΔE_{int}= -723.3 kcal mol^{-1}

ΔE_{int}= -391.4 kcal mol^{-1} ΔE_{int}= -686.0 kcal mol^{-1}

Fig. 4. Models of the bidentate-mononuclear complex (a and b) and bidentate-binuclear complex (c and d) for Sb(V) adsorbed on Fe (oxyhydr)oxide and Mn oxide (H = white and O = red). (For interpretation of the references to colour in this figure legend, the reader is referred to the web version of this article.)

Table 4
Geochemical data for marine ferromanganese oxides.

Sample	Mn (wt%)[a]	Fe (wt%)[a]	Mn/Fe[a]	Sb (mg kg^{-1})	As (mg kg^{-1})	Sb/As	References
HG type							
AD14	13.4	11.7	1.15	29.3	194	0.15	Kashiwabara et al., 2014
D535	12.8	12.7	1.01	26.6	157	0.17	Kashiwabara et al., 2014
CD25	13.1	12.1	1.08	24.4	116	0.21	This study
D886	18.5	19	0.97	22.7	144	0.16	This study
Mean ± SD	14.5 ± 2.70	13.9 ± 3.40	1.10 ± 0.10	25.7 ± 2.9	153 ± 32.5	0.17 ± 0.03	This study
				13.0–48.8	9.0–385		Usui and Someya, 1997
DG type							
FG352	25.9	6.07	4.27	35	44.8	0.78	This study
B6	25.6	5.3	4.83	40.7	146	0.28	This study
G181	29.4	4.68	6.28	24	125	0.19	This study
FG243-1	26.8	4.2	6.38	38.7	44.9	0.86	This study
Mean ± SD	26.9 ± 1.70	5.10 ± 0.80	5.40 ± 1.10	34.6 ± 7.5	90.3 ± 53.2	0.53 ± 0.34	This study
				10.4–65.2	56.0–334		Hein et al., 2012
HT type							
D12-X2	44.2	0.08	553	44.5	16.8	2.66	This study
				0.8–130	0.8–160		Usui and Someya, 1997

[a] These data are obtained from Takahashi et al. (2007).

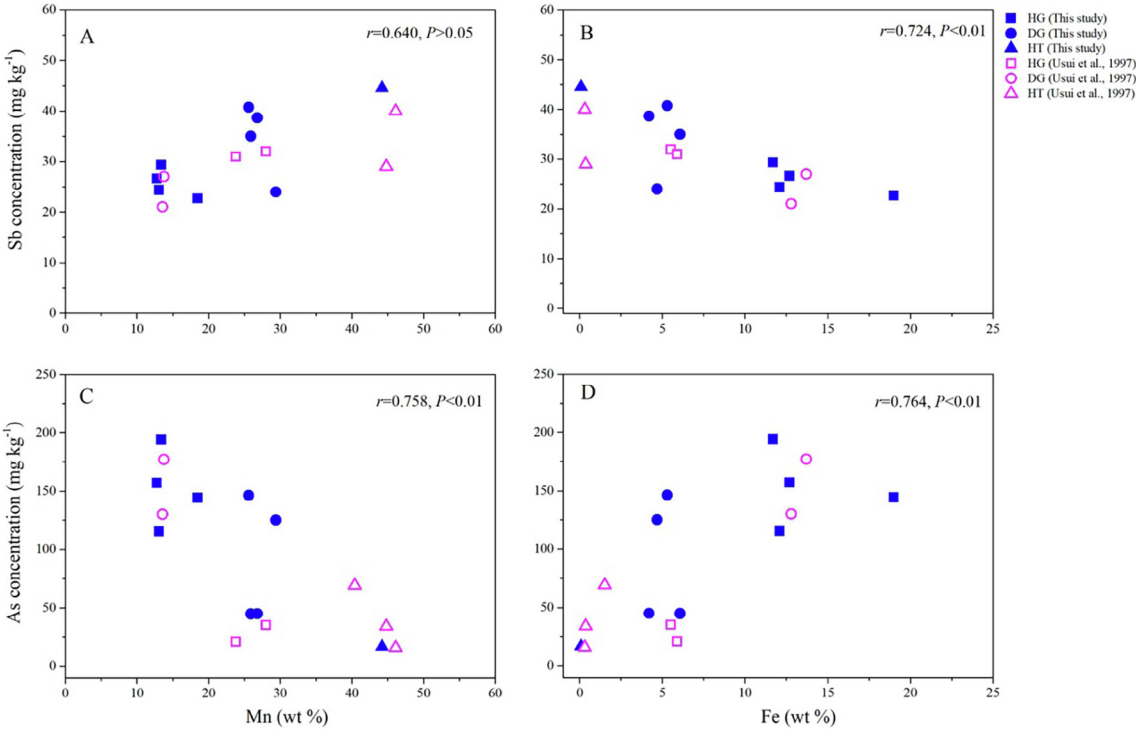

Fig. 5. Sb and As concentration as a function of Mn or Fe content for marine ferromanganese oxides.

parameters were attempted to be obtained with a three-shell model consisting of the Sb–O and two Sb–Fe/Mn shells (Table 6). For the samples containing higher proportions of Sb(V)-adsorbed ferrihydrite (D535, D886, and B6), the distant peaks were well simulated by the Sb–Mn shell at 3.00–3.05 Å and the Sb–Fe shell at 3.54–3.58 Å in addition to the prominent Sb–O peak at ~ 1.98 Å. By comparison, the best fit for the EXAFS spectrum of F243-1 was composed of the shorter Sb–Fe shell at 3.09 Å and the longer Sb–Mn shell at 3.46 Å (Table 6).

3.4.4. As EXAFS spectra for selected ferromanganese samples

Fig. 9A shows that the $k^3\chi(k)$ spectra of As for D535 and D886 were similar to that of As(V)-adsorbed ferrihydrite, despite a small difference for the two hydrogenetic fer-

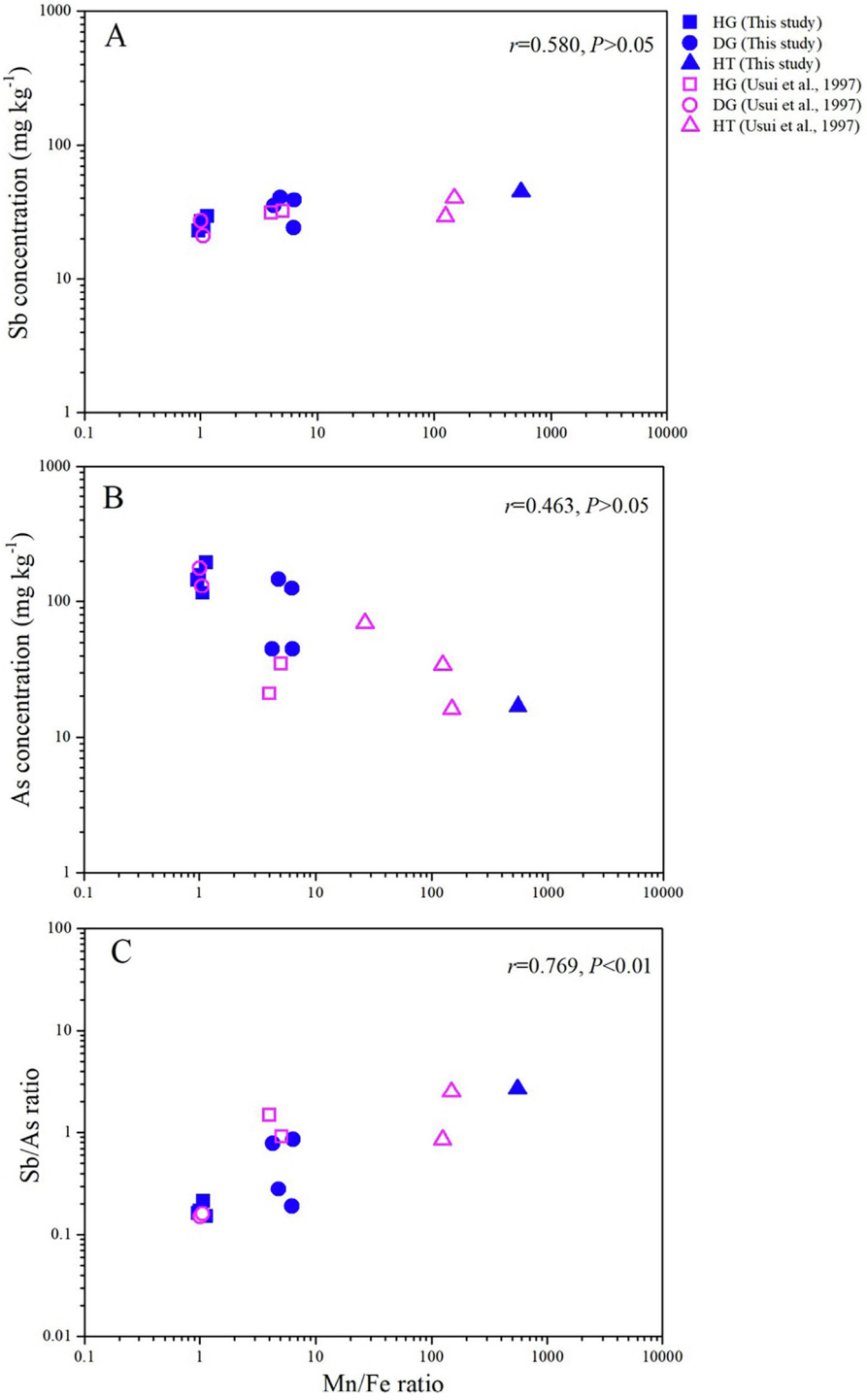

Fig. 6. The Mn/Fe ratio against the concentrations of Sb (A) and As (B), as well as the Sb/As ratio (C) for marine ferromanganese oxides.

romanganese samples. The dominant As(V)-adsorbed ferrihydrite (86%–95%) and considerably smaller amounts of As (V)-adsorbed δ-MnO_2 (5%–14%) were estimated for As speciation in the two samples via LCF analysis (Table 7). Likewise, the diagenetic sample F243-1 contained 77% As(V)-adsorbed ferrihydrite and 23% As(V)-adsorbed birnessite (Table 7). However, the remarkably different EXAFS spectrum was observed for the diagenetic sample B6 compared with other ferromanganese samples, in which the proportion of As(V)-adsorbed birnessite was equal to that of As (V)-adsorbed ferrihydrite (Fig. 9A and Table 7).

Similar to As(V)-adsorbed ferrihydrite samples, the RSFs for D535, D886, and F243-1 were simulated with the As–O shell at a distance of 1.69 Å and the As-Fe shell at a similar distance (3.24–3.27 Å), which are highly comparable to those reported previously by Yang et al. (2019).

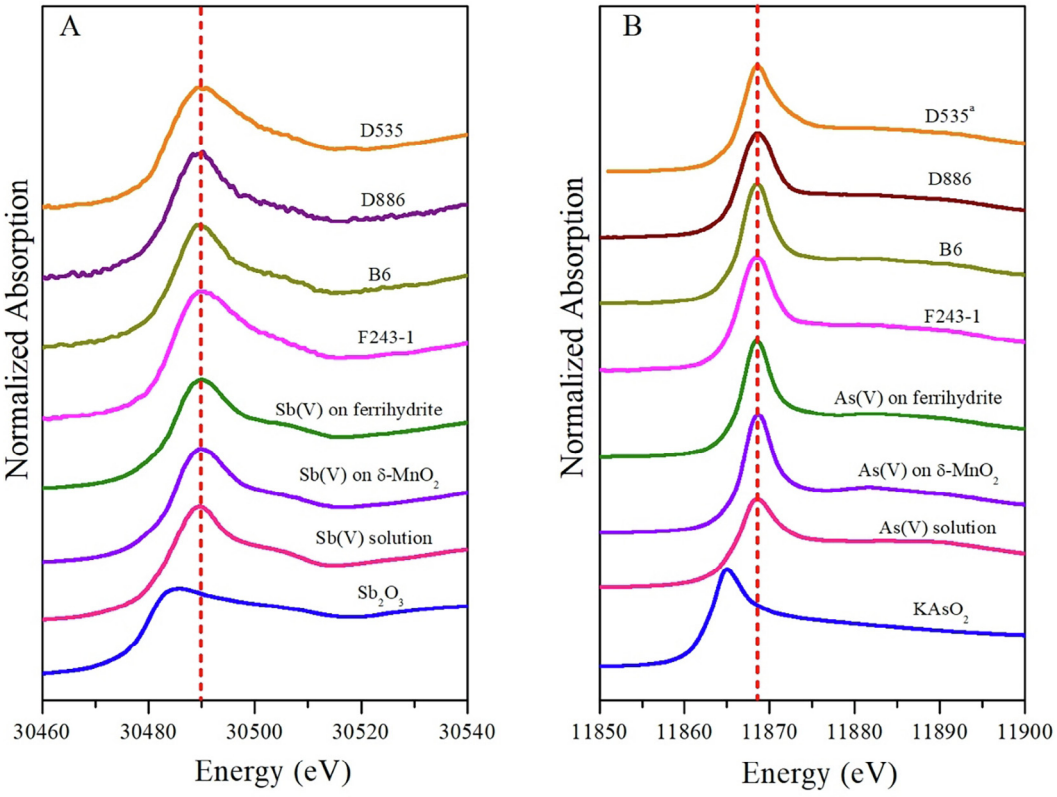

Fig. 7. Sb (A) and As (B) K-edge XANES spectra for a selection of marine ferromanganese oxides and reference materials. ([a] The As XANES data of D535 was referred to Yang et al. (2019)).

Although we simulated the further distant peak in the RSF of sample B6 by the As–Fe shell at a shorter distance of 3.21 Å (Table 7), this peak may also be contributed from Mn scattering, considering the higher association of As with birnessite in this sample derived from the LCF analysis. More appropriate models may be required to improve the fit quality.

4. DISCUSSION

4.1. Surface complexations of Sb and As on Fe/Mn (oxyhydr) oxides

Numerous studies have suggested that both Sb(V) and As(V) can be strongly adsorbed on various Fe and Mn (oxyhydr)oxides via inner-sphere complexation through surface complex modeling and direct observation revealed by EXAFS analysis (e.g., Waychunas et al., 1993; Foster et al., 2003; Ona-Nguema et al., 2005; Mitsunobu et al., 2006, 2010; Villalobos et al., 2014). Recently, the $p\bar{K}_a$($p\bar{K}_a = (pK_{a1} + pK_{a2})/2$) model was proposed to predict the attachment modes for the adsorption of oxyanions, such as Te, Se, W, and Mo onto ferrihydrite, because the surface complex constants for oxyanions onto metal oxides are largely dependent on the pK_a of conjugate acids (Takahashi et al., 2015; Qin et al., 2017a). According to this model, As(V) is inclined to form an inner-sphere complex on ferrihydrite (Qin et al., 2017a), although Sb(V) is impossible to predict because the $Sb^V(OH)_6^-$ species only has one proton dissociation constant. These previous results from theoretical prediction and spectroscopic observation are consistent with our EXAFS analyses, showing that the inner-sphere complexes are formed on the surface of ferrihydrite, δ-MnO_2, and birnessite for Sb(V) and As(V).

4.1.1. Structures of Sb(V) on ferrihydrite, δ-MnO_2, and birnessite

The simulated distances for the short and long Sb–Fe/Mn shells obtained from our EXAFS analyses (Table 2) agree with the theoretical distances between the Sb and Fe/Mn atoms in the bidentate–mononuclear and bidentate–binuclear complexes by DFT calculations, respectively (Fig. 4). This consistency clearly reveals that Sb(V) can be adsorbed on the surface of ferrihydrite and Mn oxides with the formation of both bidentate–mononuclear and bidentate–binuclear complexes, which is consistent with the previous studies (e.g., Mitsunobu et al., 2010). Similar findings have been reported for various metal(loid)s, such as Se, Cd, Pb, and Te (e.g., Waychunas et al., 1993; Manceau, 1995; Takahashi et al., 2007; Kashiwabara et al., 2014; Qin et al., 2017a).

Furthermore, the proportion of the bidentate-mononuclear and bidentate-binuclear complex was estimated on the basis of the coordination numbers ratio of the two Sb–Fe/Mn shells obtained at the same Debye–Waller factor, as described in previous studies (Takahashi et al., 2007; Kashiwabara et al., 2011). According to this calculation, the proportion of the two surface complexes is not

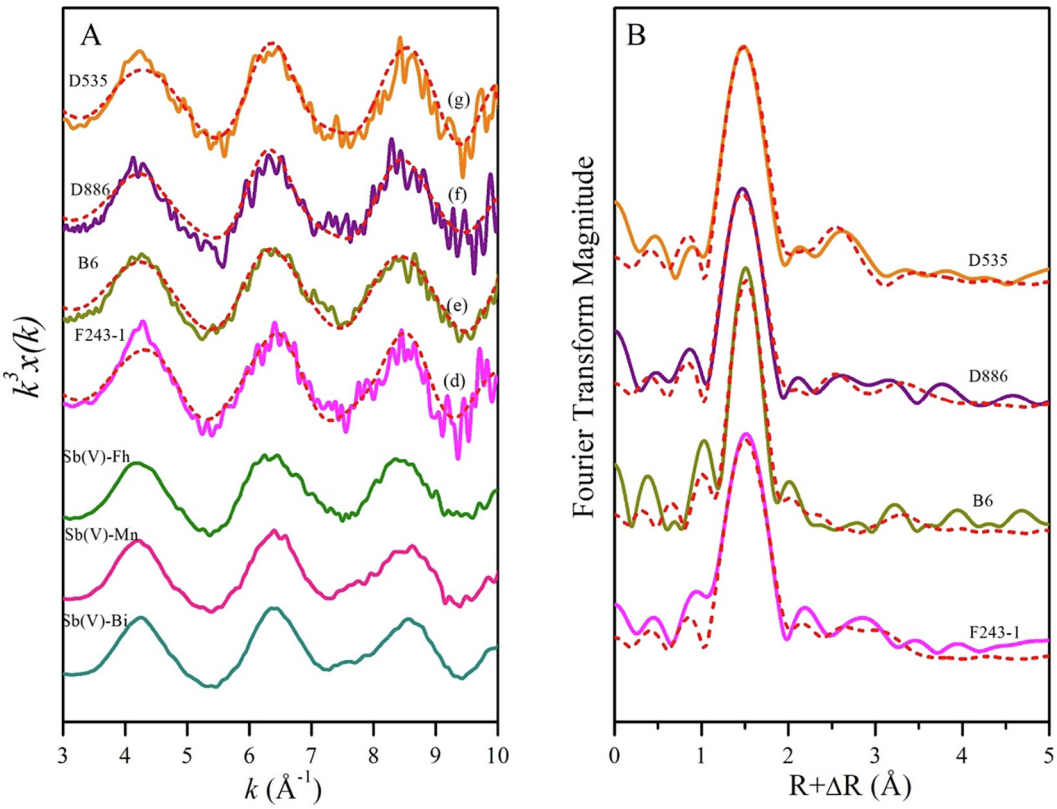

Fig. 8. Sb K-edge $k^3\chi(k)$ spectra (A) and the RSFs (B) for marine ferromanganese oxides. Solid lines are spectra obtained by experiments, while red dash lines in the $k^3\chi(k)$ spectra and RSFs are calculated data obtained by the LCF and curve-fitting analysis, respectively. (Sb(V)-Fh: Sb(V) adsorbed on ferrihydrite; Sb(V)-Mn: Sb(V) adsorbed on δ-MnO_2; Sb(V)-Bi: Sb(V) adsorbed on birnessite). (For interpretation of the references to colour in this figure legend, the reader is referred to the web version of this article.)

Table 5
The LCF results for the $k^3\chi(k)$ spectra of Sb in selected marine ferromanganese samples.

Sample	Sb(V)-adsorbed ferrihydrite (%)	Sb(V)-adsorbed δ-MnO_2 (%)	Sb(V)-adsorbed birnessite (%)
D535	86 ± 18	14 ± 12	–
D886	71 ± 19	29 ± 14	–
B6	73 ± 15	–	27 ± 8
F243-1	46 ± 16	–	54 ± 20

Table 6
Structural parameters of Sb in a selection of marine ferromanganese oxides obtained by a curve-fitting analysis of EXAFS spectra.

Sample	Shell	CN	R (Å)	ΔE_0 (eV)	σ^2 (Å^2)	R factor (%)
D535	Sb-O	6.6(0.4)	1.98(0.01)	8.09	0.001	3.59
	Sb-Mn	1.8(0.6)	3.05(0.02)		0.003	
	Sb-Fe	1.2(0.9)	3.56(0.06)		0.003	
D886	Sb-O	6.5(0.4)	1.98(0.01)	6.51	0.001	1.99
	Sb-Mn	1.2(0.5)	3.01(0.03)		0.003	
	Sb-Fe	2.6(0.8)	3.54(0.02)		0.003	
B6	Sb-O	6.4(0.4)	1.97(0.01)	5.52	0.002	2.02
	Sb-Mn	0.4(0.5)	3.00(0.07)		0.003	
	Sb-Fe	0.9(0.7)	3.58(0.06)		0.003	
F243-1	Sb-O	6.6(0.4)	1.99(0.01)	9.21	0.001	8.39
	Sb-Fe	0.2(0.7)	3.09(0.08)		0.003	
	Sb-Mn	1.3(0.8)	3.46(0.05)		0.003	

The estimated errors (standard deviations) are given in parentheses.

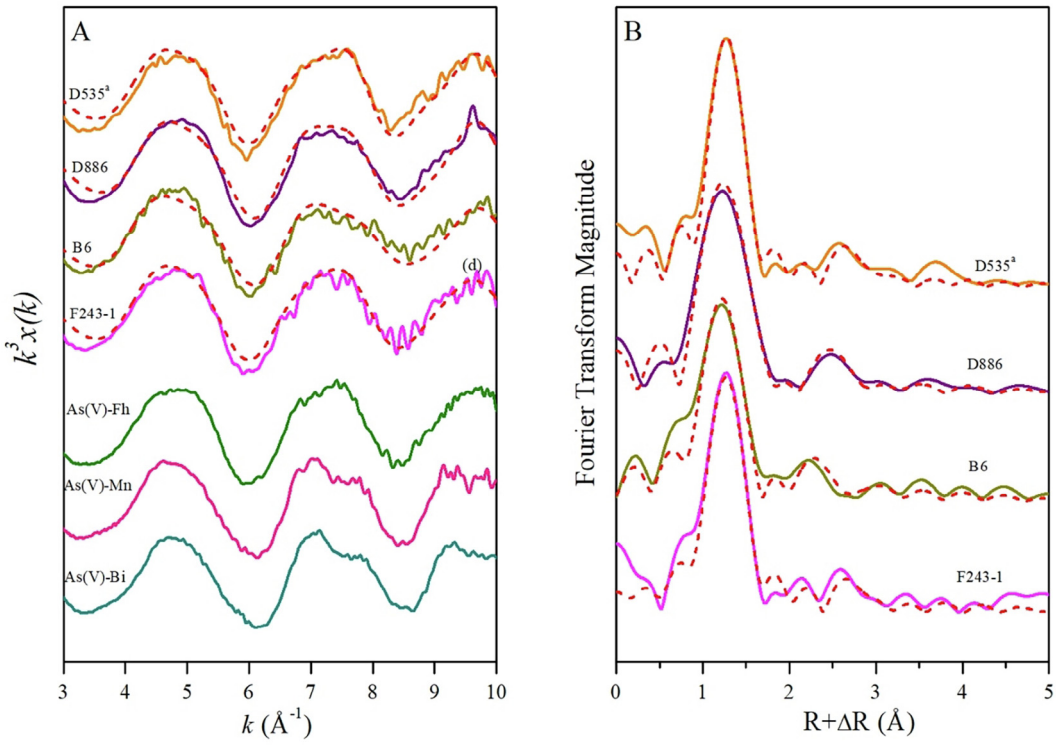

Fig. 9. As K-edge $k^3\chi(k)$ spectra (A) and the RSFs (B) for marine ferromanganese oxides. Solid lines are spectra obtained by experiments, while red dash lines in the $k^3\chi(k)$ spectra and RSFs are calculated data obtained by the LCF and curve-fitting analysis, respectively. ([a] The As EXAFS data of D535 was referred to Yang et al (2019). As(V)-Fh: As(V) adsorbed on ferrihydrite; As(V)-Mn: As(V) adsorbed on δ-MnO_2; As(V)-Bi: As(V) adsorbed on birnessite). (For interpretation of the references to colour in this figure legend, the reader is referred to the web version of this article.)

Table 7
The LCF results for the $k^3\chi(k)$ spectra of As in selected marine ferromanganese samples.

Sample	As(V)-adsorbed ferrihydrite (%)	As(V)-adsorbed δ-MnO_2 (%)	As(V)-adsorbed birnessite (%)
D535	95 ± 9	5 ± 5	-
D886	86 ± 9	14 ± 5	-
B6	50 ± 12	-	50 ± 9
F243-1	77 ± 10	-	23 ± 7

pronouncedly different for Sb(V) adsorbed on ferrihydrite at different loading levels, possibly implying that the variation of surface complex species of Sb(V) on ferrihydrite is independent of surface coverage (Mitsunobu et al., 2010). This finding can be supported by the similar ΔE_{int} values for the two complexes on Fe (oxyhydr)oxide from the DFT calculations. Hence, Sb(V) could be evenly adsorbed on the edge sites at chain terminations and planes sites in ferrihydrite via edge-sharing and corner-sharing complexations, respectively.

However, in terms of Sb(V) adsorption on δ-MnO_2 and birnessite, bidentate–mononuclear complex (57%–82%) was predominant based on the ratio of $CN_{Sb\text{-}Mn1}$ and $CN_{Sb\text{-}Mn2}$, suggesting that the lateral sites of Mn oxides seem to be favorable for Sb(V). This finding can be well explained by the fact that the structure and the O–O bond length of the octahedron $Sb^V(OH)_6^-$ are similar to the octahedron MnO_6 unit of Mn oxides, resulting in Sb(V) being preferentially adsorbed at layer edges in Mn oxides with the formation of edge-sharing complexes. This is further confirmed by the relative stability predicted by the DFT calculations, showing that the bidentate–mononuclear complex is energetically favorable and more stable because of its much lower ΔE_{int} compared with the bidentate–binuclear complex on Mn oxide.

Interestingly, the proportion of the bidentate–mononuclear complex on δ-MnO_2 is gradually decreased from 82% to 69% with increased Sb/Mn ratio, but those for birnessite (57%) became smaller. To demonstrate the difference between Sb(V) on birnessite and on δ-MnO_2 at different loading levels, we subtracted out the fitted first Sb–O shell contribution from their $k^3\chi(k)$ data and reperformed the Fourier transform to obtain higher shells. As shown in Fig. S3, the longest distance for the higher shell was observed for Sb(V)-adsorbed birnessite compared with δ-MnO_2, and this distance became slightly longer for

Sb(V)-adsorbed δ-MnO_2 with increased Sb/Mn ratio. Considering that the distance between Sb and Mn in the bidentate–binuclear complex is longer than that in the bidentate–mononuclear complex, the longer distance for the higher shell can be due to a larger contribution from the bidentate-binuclear complex. These results clearly indicate that the surface complexations are somewhat different among Sb(V)-adsorbed birnessite and δ-MnO_2 at different loading levels. This discrepancy can be interpreted from the crystal structures of δ-MnO_2 and birnessite. The birnessite has larger layers and well-ordered stacking of the layers in the (001) direction, and thus has a higher proportion of basal sites to lateral sites compared with δ-MnO_2, because the crystals of Mn minerals are formed by sharing lateral sites within each layer (Manceau et al., 2002, 2007; Foster et al., 2003; Villalobos et al., 2003; Takahashi et al., 2007). Consequently, more corner-sharing complexes would be formed at the basal sites dominated in birnessite once the lateral sites are occupied by Sb(V). By contrast, Sb(V) can be mostly adsorbed on layer edges in δ-MnO_2 to form a relatively stable bidentate–mononuclear complex, but the bidentate–binuclear complex may also be formed after the saturation of the edge-sharing sites of δ-MnO_2 based on the gradually increased proportion of bidentate–binuclear complex for δ-MnO_2 with increased Sb loading.

4.1.2. Structures of As(V) on ferrihydrite, δ-MnO_2, and birnessite

In the present study, the distances of the As–Fe/Mn shell for adsorbed samples obtained from EXAFS analysis (Table 3) are quite comparable to those for the bidentate–binuclear complex predicted by our DFT calculations (Fig. S4), suggesting that the bidentate–binuclear complex is the main attachment mode for As(V) adsorption on ferrihydrite, δ-MnO_2, and birnessite. Despite the possible presence of the bidentate–mononuclear (edging-sharing) complex having a shorter As–Fe distance (Fig. S4), this complex is substantially energetically unfavorable compared with the bidentate–binuclear complex based on their considerably large energy difference (Sherman and Randall, 2003). Moreover, the peak at ~ 2.85 Å in the RSFs may also result from the As–O–O multiple scattering for AsO_4 tetrahedron, because the weak second neighbor for As(V)-adsorbed samples (e.g., As–Fe shell) may become ambiguous due to the contribution from the strong first neighbor (Sherman and Randall, 2003; Ona-Nguema et al., 2005). Sherman and Randall (2003) reported that the coordination number of the As–Fe shell corresponding to the bidentate-mononuclear complex should be very small (<0.3) when multiple scattering is accounted for, thereby indicating that such a complex need not be included. On this basis, numerous studies have included the As–O–O path during the EXAFS analysis for the laboratory adsorbed and natural ferromanganese samples (e.g., Ona-Nguema et al., 2005; Manceau et al., 2007; Yang et al., 2019). Thus, As(V) is mostly adsorbed on the surface of ferrihydrite through the bidentate–binuclear complexation.

Unlike Sb(V), As(V) can be preferentially adsorbed on δ-MnO_2 and birnessite with the formation of bidentate–binuclear complexes. The discrepancy on surface complexations for the two elements on Mn oxides can be attributed to the geometric differences of the octahedron $Sb^{V}(OH)_6^-$ and tetrahedron $As^{V}O_4^{3-}$. In contrast to $Sb^{V}(OH)_6^-$, the tetrahedron $As^{V}O_4^{3-}$ is difficult to bind with the lateral sites of the octahedron MnO_6, resulting in the corner-sharing (bidentate–binuclear) complex being preferentially formed at the basal sites in δ-MnO_2 and birnessite.

4.2. Distribution and speciation of Sb and As in marine ferromanganese oxides

The associations of trace elements in ferromanganese oxides have been assessed by interelement correlations and factor analyses of bulk chemical composition (Li, 1982), in which Sb and As were speculated to be preferentially concentrated in Mn oxides and Fe oxides in abyssal Pacific ferromanganese nodules, respectively. Nonetheless, this statistical method should be viewed cautiously, because it may be problematic for elements that are enriched in more than one phase (Koschinsky and Hein, 2003; Takahashi et al., 2007). In the present study, the distribution and speciation of Sb and As in different types of marine ferromanganese oxides were further understood by estimating the associations of the two elements with Fe and Mn oxide phases based on their EXAFS spectra. To the best of our knowledge, the Sb EXAFS analyses for different types of marine ferromanganese oxides are herein reported for the first time.

4.2.1. Distribution of Sb in marine ferromanganese oxides

The LCF result of EXAFS data showed that Sb is mostly associated with ferrihydrite in hydrogenetic samples (Table 5), revealing that the Fe oxide component appears to be the main host phase of Sb in marine ferromanganese oxides. This finding is in good agreement with the sequential extraction results showing that most of Sb is present in the Fe (oxyhydr)oxide fraction for hydrogenetic ferromanganese samples (e.g., Koschinsky and Hein, 2003). Recently, the similar distribution pattern between Sb and Fe has been observed in a hydrogenetic ferromanganese sample by micro-focused X-ray fluorescence (μ-XRF) analysis (Kashiwabara et al., 2014), which provides direct evidences for the strong associations of Sb with Fe oxide component.

Interestingly, some amounts of Sb can also be associated with Mn oxides in marine ferromanganese samples by EXAFS analysis in this study (Table 5). The highest proportion of Sb adsorbed on birnessite (54%) was found in the diagenetic sample F243-1 having a relatively high Mn/Fe ratio (6.38) (Table 5). This result seems to be supported by the positive correlation between Sb and Mn/Fe ratio in ferromanganese samples (Fig. 6). We speculate that a much higher proportion of Sb would be hosted by Mn oxides in the hydrothermal samples with the highest Mn/Fe ratios, although the corresponding EXAFS spectra were not obtained because of insufficient sample. In fact, this assumption can be verified by the previous study showing a large amount of Sb can be extracted in the Mn oxide fraction in hydrothermal ferromanganese oxides using sequential extraction method (Koschinsky and Hein, 2003).

Previous studies have demonstrated that Mn oxides can be the main host phase for various oxyanions, such as W and Mo in marine ferromanganese oxides, which is attributed to the relatively high stability for the formed inner-sphere complex on Mn oxides (Kashiwabara et al., 2011, 2013; Yang et al., 2019). Considering the formation of stable inner-sphere complexes on the surface of Mn oxides indicated by the EXAFS analysis in this study, thus, negatively charged Mn oxides should be expected to be an important host phase for Sb (main dissolved species: $Sb(OH)_6^-$) despite the presence of positively charged Fe oxides in marine ferromanganese oxides, especially for the samples with high Mn/Fe ratio.

Moreover, the mineral composition is one of important controlling factors for the distribution of various trace elements in ferromanganese oxides (Koschinsky and Hein, 2003; Takahashi et al., 2007; Liu et al., 2017). According to the LCF result, Sb species associated Mn oxide components in the diagenetic samples is birnessite in contrast to δ-MnO_2 in the hydrogenetic samples (Table 5). This finding can be supported by the fact that vernadite (corresponding to synthetic δ-MnO_2) and birnessite are the main Mn minerals in the hydrogenetic and diagenetic marine ferromanganese samples, respectively, while the main Fe oxide component is speciated as ferrihydrite (Takahashi et al., 2007; Yang et al., 2019). Therefore, our study clearly reveal that the constituent Mn oxides play a key role for the distribution of Sb in different types of marine ferromanganese oxides.

In this study, we attempted to obtain the specific attachment mode for Sb in marine ferromanganese oxides by a curve-fitting analysis. It is worth noting that these structural parameters should be cautiously viewed and explained, considering the coexistence of Fe and Mn phases in natural ferromanganese oxides and their similar EXAFS scattering functions. However, the distance of the Sb–Mn shell is slightly shorter than that of the Sb–Fe shell for each surface complex mode, which may be attributed to the smaller ionic radius of Mn^{4+} (0.53 Å) compared with Fe^{3+} (0.64 Å). This reduction in distance has been justified to identify the mineral host and chemical bonding mode for various metal(loid)s, such as As and Pb (Manceau et al., 2007; Takahashi et al., 2007). In addition, the surface complexations are significantly different for Sb adsorbed on ferrihydrite, δ-MnO_2, and birnessite as indicated by EXAFS analysis, hence, our shell-by-shell fit results are somewhat reasonable considering the main attachment modes for Sb on the constituent minerals in marine ferromanganese oxides. For example, the optimized fitting model consisting of the shorter Sb–Fe shell and longer Sb–Mn shell for F243-1 was obviously different from those for other ferromanganese samples, which may be ascribed to the stronger association of Sb(V) with the basal sites in the constituent birnessite, whereas the lateral sites in δ-MnO_2 are favorable for Sb in the hydrogenetic samples.

4.2.2. Distribution of As in marine ferromanganese oxides

Numerous studies have documented that As is selectively associated with the Fe oxide component in ferromanganese samples through various approaches, such as interelemental correlations, sequential extraction, μ-XRF, and XAFS techniques (e.g., Li, 1982; Koschinsky and Hein, 2003; Marcus et al., 2004; Manceau et al., 2007; Mitsunobu et al., 2006; Yang et al., 2019). In this study, we found that the As(V)-adsorbed ferrihydrite is predominant in natural ferromanganese oxides (Table 7). Despite only 50% of As(V)-adsorbed ferrihydrite fraction in the diagenetic sample B6, its contribution is still large considering that the Mn/Fe ratio (4.83) is much higher compared with other hydrogenetic samples. Meanwhile, the optimized structural parameters for the As EXAFS data of marine ferromanganese are highly similar to those for As(V)-adsorbed ferrihydrite (Table 8) and natural ferromanganese coatings on quartz (Manceau et al., 2007). Considering that Fe mostly occurs as ferrihydrite (e.g., Marcus et al., 2004, Takahashi et al., 2007, Yang et al., 2019), one can conclude that As is predominantly adsorbed on the plane sites of ferrihydrite in marine ferromanganese oxides via the formation of bidentate-binuclear complexes.

Table 8
Structural parameters of As in marine ferromanganese oxides obtained by a curve-fitting analysis of EXAFS spectra.

Sample	Shell	CN	R (Å)	ΔE_0 (eV)	σ^2 (Å^2)	R factor (%)
D535	As-O	4.5(0.4)	1.69(0.01)	5.81	0.003	3.14
	As-O-O	12[a]	3.10		0.003	
	As-Fe	1.6(1.1)	3.27(0.05)		0.008	
D886	As-O	4.6(0.4)	1.69(0.01)	8.68	0.003	3.86
	As-O-O	12[a]	3.10		0.003	
	As-Fe	1.1(1.1)	3.25(0.07)		0.008	
B6	As-O	4.7(0.4)	1.68(0.01)	4.28	0.004	7.48
	As-O-O	12[a]	3.10		0.004	
	As-Fe/Mn	1.4(1.0)	3.21(0.08)		0.009	
F243-1	As-O	4.6(0.4)	1.69(0.01)	5.19	0.003	3.59
	As-O-O	12[a]	3.10		0.003	
	As-Fe	1.1(1.4)	3.24(0.09)		0.008	

The estimated errors (standard deviations) are given in parentheses.

[a] Fixed to be 12 for $CN_{As\text{-}O\text{-}O}$ due to multiple scatting of O-O pairs in the AsO_4 tetrahedron. $\sigma^2_{As\text{-}O\text{-}O}$ is constrained to be equal to $\sigma^2_{As\text{-}O}$ during the spectral fit procedures.

Most importantly, we revealed for the first time that As is also distributed to Mn oxides in addition to Fe oxides in marine ferromanganese samples by using EXAFS analysis. Similar findings have reported in several laboratory experiments and natural samples from surface environments (e.g., Frierdich and Catalano, 2012; Ying et al., 2012; Liu et al., 2017). Ying et al. (2012) indicated that As tends to complex with birnessite rather than goethite at high As concentrations in a laboratory experiment. Frierdich and Catalano (2012) observed that As correlates with Fe and Mn in ferromanganese oxides from shallow karst cave systems. More recently, pyrolusite has also been suggested to be an important sink of As in ferromanganese duricrust covering carboniferous carbonates at the Qixia Mountain in Eastern China (Liu et al., 2017). These results confirm our finding that Mn oxides can also be the host phase of As in marine ferromanganese samples, especially for the diagenetic and hydrothermal types with higher Mn/Fe ratio.

4.3. Comparison between the enrichment of Sb and As in marine ferromanganese oxides

On the basis of macroscopic adsorption experiments and EXAFS analyses, we accordingly attempted to clarify the mechanisms for different enrichment factors of the two elements in marine ferromanganese oxides at the molecular level. The macroscopic adsorption experiments showed different inhibition effects for Sb(V) and As(V) on ferrihydrite/δ-MnO_2 in the ASW system compared with the MQ water system (Fig. 1), which is likely attributed to the presence of coexisting anions, such as sulfate (SO_4^{2-}) and bicarbonate (HCO_3^-) in artificial seawater.

Previous studies have reported that the adsorption of As (V) on ferrihydrite significantly decreases in the presence of sulfate or bicarbonate (e.g., Wilkie and Hering, 1996; Jain and Loeppert, 2000; Frau et al., 2010), probably owing to their great competition with the adsorbed sites for As(V). More recently, a study has demonstrated that sulfate can form the bidentate–binuclear inner-sphere complex on the surface of ferrihydrite (Gu et al., 2016). Similarly, a large amount of inner-sphere complexes can also be formed on ferrihydrite surface for bicarbonate by the theoretical prediction and spectroscopic observations (Appelo et al., 2002; Frau et al., 2010; Qin et al., 2017a). According to the EXAFS results, As(V) is also readily adsorbed on basal sites rather than lateral sites in both ferrihydrite and δ-MnO_2 via bidentate-binuclear complexations. Therefore, the adsorption sites of As(V) would compete with coexisting sulfate and bicarbonate in artificial seawater because of their similar bidentate–binuclear complexations, resulting in the pronounced reduction of As(V) adsorption on ferrihydrite and δ-MnO_2 in the ASW system.

By comparison, the sulfate and bicarbonate anions showed a significant competition with Sb(V) on ferrihydrite surface (e.g., Wu et al., 2010), but this effect was not pronounced for Sb(V) adsorption on Mn oxides (e.g., Essington and Vergeer, 2015). Similar results were observed in Sb(V) adsorption on ferrihydrite and δ-MnO_2 in the ASW system in the present study. The discrepancy on the adsorption of Sb(V) on ferrihydrite and δ-MnO_2 in the ASW system can be explained from the structures of surface complexes. Our EXAFS analyses indicate that similar amounts of bidentate–binuclear and bidentate–mononuclear complexes can be formed on the plane sites and edge sites in ferrihydrite for Sb(V), respectively, whereas Sb(V) prefers to bind with the lateral sites in δ-MnO_2 via the stable bidentate–mononuclear complexation rather than the bidentate–binuclear complexation. Considering the predominant formation of bidentate-binuclear complexes for sulfate and bicarbonate on ferrihydrite and δ-MnO_2, the preferential lateral sites in δ-MnO_2 for Sb(V) would slightly compete with coexisting sulfate and bicarbonate in artificial seawater, resulting in a much less inhibition effect for Sb(V) adsorption on δ-MnO_2 compared with ferrihydrite in the ASW system. Consequently, the structural information derived from the EXAFS data provides the molecular-scale insights into the different adsorption behaviors for Sb(V) and As(V) on ferrihydrite or δ-MnO_2 in the ASW system, which can be extended to understand the geochemical behaviors and fates of the two elements in natural marine environments.

For hydrogenetic ferromanganese oxides in natural marine environments, the adsorption of $As^VO_4^{3-}$ on the basal sites in constituent ferrihydrite and δ-MnO_2 may be significantly inhibited by the large competition of coexisting sulfate and bicarbonate in seawater. Although the coexisting anions also have some influence on the adsorption of $Sb^V(OH)_6^-$ on ferrihydrite, the inhibition effect for $Sb^V(OH)_6^-$ on δ-MnO_2 is considerably smaller because less competition exists for the favorable lateral sites. Hence, the larger inhibition effects for As may lead to the enrichment factor of As being much lower than that of Sb in hydrogenetic ferromanganese oxides.

Moreover, with increased Mn/Fe ratio, the difference in enrichment factor between Sb and As enlarges, which is supported by the positive correlation between Sb/As and Mn/Fe ratios in marine ferromanganese samples (Fig. 6C). In terms of diagenetic ferromanganese oxides with higher Mn/Fe ratios, the adsorption of Sb on the basal sites in birnessite (the main constituent Mn oxide) may also be subject to the similar inhibition effect to some degree. Nevertheless, a part of $Sb^V(OH)_6^-$ can form bidentate–mononuclear complexes on the lateral sites in birnessite, which is not significantly competed with coexisting anions in seawater. Considering a remarkable inhibition for $As^VO_4^{3-}$ on Mn oxides under seawater condition, the enrichment degree of Sb becomes even larger than that of As in diagenetic ferromanganese samples. Therefore, different surface complexations on constituent Fe and Mn oxides provide molecular-scale insights into the larger enrichment of Sb than As in ferromanganese oxides from marine environment.

4.4. Factors controlling the enrichment of oxyanions in marine ferromanganese oxides: highlights on the structural similarity

According to the adsorption model suggested by previous researchers (James and Healy, 1972; Koschinsky and Hein, 2003), the change in the Gibbs free energy during

the adsorption of ions on solids (ΔG_{ads}) includes the contributions from the Coulombic electrostatic interaction (ΔG_{coul}), the specific chemical interaction (ΔG_{chem}), and the secondary solvation or hydration (ΔG_{solv}): $\Delta G_{ads} = \Delta G_{coul} + \Delta G_{chem} + \Delta G_{solv}$.

In deep seawater at circumneutral pH, the surface of δ-MnO_2 is negatively charged given its low pH_{pzc} (point of zero charge) value (1.3–2.8), while Fe (oxyhydr)oxides have a slightly positive charge (Langmuir, 1997; Koschinsky and Hein, 2003). Thus, the ΔG_{coul} is generally considered to be vital for the enrichment of cations in negatively charged Mn oxide phase due to electrostatic interaction, whereas the ΔG_{chem} derived from chemical interaction plays a more important role compared with ΔG_{coul} for negatively charged ions on the Fe oxide component with a slightly positive charge. Similarly, the ΔG_{chem} should also be of great significance for the enrichment of negatively charged oxyanions (e.g., W and Mo) in marine ferromanganese oxides, in which the host phases of W and Mo have been identified as negatively charged Mn oxide components (Kashiwabara et al., 2011, 2013, Yang et al., 2019). The EXAFS results suggested that W and Mo can be mainly adsorbed on Mn oxide through the a strong inner-sphere complexation (chemical interaction), and the larger enrichment of W compared with Mo in marine ferromanganese oxides is likely due to their stability of inner-sphere complexes on Mn oxide and different attachment modes on ferrihydrite (Kashiwabara et al., 2011, 2013).

Furthermore, several other mechanisms have been proposed to interpret the enrichment of specific oxyanions in marine ferromanganese oxides, as described below. One mechanism is surface oxidation, which has been documented to be reasonable for some cations, such as Co and Ce, because the oxidized forms of Co(III) and Ce(IV) are highly insoluble and thus are progressively enriched in ferromanganese oxide (Murray and Dillard, 1979; Takahashi et al., 2007, Koschinsky and Hein, 2003). This redox reaction has also been used to explain the extreme enrichment of Te oxyanion in marine ferromanganese samples (Hein et al., 2003; Koschinsky and Hein, 2003). Nonetheless, only the oxidation of oxyanion Te(IV) to Te (VI) by Mn oxides does not likely result in such high Te enrichment due to the high solubility of Te(VI), but this process can provide extra Te(VI) for its structural incorporation into the Fe oxide phase in ferromanganese oxides (Kashiwabara et al., 2014). Considering that the oxidized forms of Sb(V) and As(V) are the predominant species in seawater and ferromanganese deposits, surface oxidation is probably not the main process for the enrichment of Sb and As in marine ferromanganese oxides.

More recently, the structural incorporation of Te(VI) into the Fe oxide phase through coprecipitation has been identified as the main chemical process for the extreme enrichment of Te in ferromanganese oxides because of the geometric similarity of the Te(VI) molecule and the Fe octahedron in ferrihydrite (Kashiwabara et al., 2014, Qin et al., 2017a). For Sb and As studied in this work, several laboratory studies reported that As(V) and Sb(V) can also be structurally incorporated in Fe (oxyhydr)oxides (e.g., Fuller et al., 1993; Violante et al., 2007; Mitsunobu et al., 2010; Tokoro et al., 2010). However, it seems to be unlikely for the structural incorporation of As into Fe oxides in natural ferromanganese oxides because of the extremely slow growth rate (mm/Ma) (Hein et al., 2003), considering that the tetrahedral $As^{V}O_4^{3-}$ would be excluded from linkages of the Fe octahedral after a long aging time (Fuller et al., 1993; Waychunas et al., 1993; Kashiwabara et al., 2014). In the case of Sb, if Sb were enriched in marine ferromanganese oxides through this chemical process, the enrichment factor of Sb would become as large as that of Te, but the actual observed results are remarkably lower in ferromanganese samples studied here and from other areas (e.g., Hein et al., 2003). Thus, the incorporation of Sb(V) into the crystal structure of Fe oxides is not the main mechanism for its enrichment in marine ferromanganese oxides.

In the present study, according to the surface complexes on Fe and Mn oxides, Sb can be adsorbed on the Fe oxide phase in marine ferromanganese samples via bidentate–binuclear and bidentate–mononuclear inner-sphere complexations. Meanwhile, Sb can preferentially form the bidentate-mononuclear complex on the lateral sites of constituent vernadite in hydrogenetic ferromanganese oxides, but some amounts of bidentate–binuclear complexes could also be formed on constituent birnessite in the diagenetic ferromanganese samples with higher Mn/Fe ratios. These observations are supported by the stabilities for different surface complexes derived from the interaction energy (ΔE_{int}). These findings clearly suggest that chemical factor is a crucial mechanism for Sb enrichment in marine ferromanganese oxides, especially for the negatively charged Mn oxide component having a similar octahedron structure.

By comparison, As can be preferentially adsorbed by Fe and Mn oxide component via bidentate–binuclear inner-sphere complexations, indicating that chemical interaction can also play a significant role in As enrichment in marine ferromanganese samples, in addition to electrostatic interaction as suggested by numerous previous studies (e.g., Li, 1982; Koschinsky and Halbach, 1995; Koschinsky and Hein, 2003). Notably, our finding that a part of As is also associated with negatively charged Mn oxide component highlights that chemical factor play a more important role than electrostatic interaction for As enrichment in marine ferromanganese oxides.

However, the enrichment processes and mechanisms of Sb into marine ferromanganese oxides is significantly distinct from those of As because of different structures for the two elements in seawater. In contrast to As (main dissolved species: tetrahedron $As^{V}O_4^{3-}$), Sb (main dissolved species: $Sb^{V}(OH)_6^-$) can be strongly associated with the Mn oxide component via the formation of bidentate–mononuclear complexes because of the structural similarity between octahedron $Sb^{V}(OH)_6^-$ and MnO_6, which do not significantly compete with coexisting sulfate and bicarbonate anions in seawater. Thus, our finding from this study, which highlights the structural similarity, provides a new insight into the larger enrichment of Sb compared with As in ferromanganese oxides, thereby improving the under-

standing of enrichment mechanisms and geochemical behaviors for oxyanions in marine environment at the molecular scale. Anions in seawater that have similar structures with the host phases are expected to show a larger enrichment degree in marine ferromanganese oxides, although further study is still required. Furthermore, our findings have some implications on the understanding of the contamination and mobilization of Sb and As in surface environments, such as soils and sediments, where ferrihydrite, vernadite, or ferromanganese oxides are ubiquitous.

5. CONCLUSIONS

This study provides molecular-scale insights into the enrichment mechanisms of Sb and As in marine ferromanganese oxides by combining adsorption experiments, quantum chemical calculations, and EXAFS techniques. In marine ferromanganese oxides, Sb and As can be distributed to Fe and Mn oxide components, and the disparate distribution of the two elements to Mn oxides is largely dependent on the Mn/Fe ratio and constituent minerals in different genetic types of ferromanganese deposits. In contrast to predominant bidentate-binuclear complexes for As(V) adsorbed on ferrihydrite and Mn oxides, the energetically favorable bidentate–mononuclear complex can be preferentially formed on the lateral sites in Mn oxides for Sb(V) because of the structural similarity between the octahedron $Sb^{V}(OH)_6^-$ and the MnO_6 unit. These complexes formed on the lateral sites in Mn oxides for Sb is not significantly competed with by coexisting anions in seawater, which can be partly responsible for the larger enrichment factor of Sb compared with As in ferromanganese oxides. Our study highlights that the structural similarity causes the disparate distribution and enrichment of Sb and As in marine ferromanganese oxides, thereby providing new insights into the understanding of incorporation processes and geochemical behaviors for oxyanions in marine and surface environments at the molecular level.

ACKNOWLEDGMENTS

This work was supported by the National Natural Science Foundation of China (Nos. U1732132 and 41303099),Natural Science Foundation of Guizhou Province, China ([2013]2287), Grants-in-Aid for Scientific Research from the Japan Society for the Promotion of Science (Nos. 16K05581, 17H04582, 17H06458, 18KK0296, 18H04134, 17H06455), and the "Scientific research on genesis of marine resources" for "Next-generation technology for ocean resources exploration (ZIPANG in ocean)", an initiative that is part of the "Cross-ministerial Strategic Innovation Promotion Program (SIP)" of the Japanese government. This study was performed with the approval of JASRI/SPring-8 (Nos. 2015A0118, 2016A0127, 2017A1798, 2018A0148, and 2018B1801) and Photon Factory (Nos. 2014G058 and 2015G664).

APPENDIX A. SUPPLEMENTARY MATERIAL

Supplementary data to this article can be found online at https://doi.org/10.1016/j.gca.2019.04.018.

REFERENCES

Aranda M. A. G., Bruque S. and Attfield J. P. (1991) Crystal structures and characterization of a new manganese(III) arsenate, $MnAsO_4{\cdot}1.2H_2O$, and manganese(II) pyroarsenate, $Mn_2As_2O_7$. *Inorg. Chem.* **30**, 2043–2047.

Appelo C. A. J., Van der Weiden M. J. J., Tournassat C. and Charlet L. (2002) Surface complexation of ferrous iron and carbonate on ferrihydrite and the mobilization of arsenic. *Environ. Sci. Technol.* **36**, 3096–3103.

Bau M., Schmidt K., Koschinsky A., Hein J., Kuhn T. and Usui A. (2014) Discriminating between different genetic types of marine ferromanganese crusts and nodules based on rare earth elements and yttrium. *Chem. Geol.* **381**, 1–9.

Becke A. D. (1993) Density-functional thermochemistry. III. The role of exact exchange. *J. Phys. Chem.* **98**, 5648–5652.

Berlepsch P., Armbruster T., Brugger J., GriddleA J. and Graeser S. (2003) Tripuhyite, $FeSbO_4$, revised. *Mineral. Mag.* **67**, 31–46.

Boys S. F. and Bernardi F. (1970) The calculation of small molecular interactions by the differences of separate total energies. Some procedures with reduced errors. *Mol. Phys.* **19**, 553–566.

Curtiss L. A., McGrath M. P., Blaudeau J. P., Davis N. E., Binning, Jr, R. C. and Radom L. (1995) Extension of Gaussian-2 theory to molecules containing third-row atoms Ga–Kr. *J. Chem. Phys.* **103**, 6104–6113.

Essington M. E. and Vergeer K. A. (2015) Adsorption of antimonate, phosphate, and sulfate by manganese dioxide: Competitive effects and surface complexation modeling. *Soil. Sci. Soc. Am. J.* **79**, 803–814.

Filella M., Belzile N. and Chen Y. W. (2002) Antimony in the environment: a review focused on natural waters I. *Occurrence. Earth-Sci. Rev.* **57**, 125–176.

Foster A. L., Brown G. E. and Parks G. A. (2003) X-ray absorption fine structure study of As(V) and Se(IV) sorption complexes on hydrous Mn oxides. *Geochim. Cosmochim. Acta* **67**, 1937–1953.

Frau F., Addari D., Atzei D., Biddau R., Cidu R. and Rossi A. (2010) Influence of major anions on As(V) adsorption by synthetic 2-line ferrihydrite. kinetic investigation and XPS study of the competitive effect of bicarbonate. *Water. Air. Soil. Poll.* **205**, 25–41.

Frierdich A. J. and Catalano J. G. (2012) Distribution and speciation of trace elements in iron and manganese oxide cave deposits. *Geochim. Cosmochim. Acta* **91**, 240–253.

Frisch M. J., Pople J. A. and Binkley J. S. (1984) Self-consistent molecular orbital methods 25: supplementary functions for Gaussian basis sets. *J. Chem. Phys.* **80**, 3265–3269.

Frisch M. J., Trucks G. W., Schlegel H. B., Scuseria G. E., Robb M. A., Cheeseman J. R., Scalmani G., Barone V., Mennucci B., Petersson G. A., Nakatsuji H., Caricato M., Li X., Hratchian H. P., Izmaylov A. F., Bloino J., Zheng G., Sonnenberg J. L., Hada M., Ehara M., Toyota K., Fukuda R., Hasegawa J., Ishida M., Nakajima T., Honda Y., Kitao O., Nakai H., Vreven T., Montgomery, Jr, J. A., Peralta J. E., Ogliaro F., Bearpark M., Heyd J. J., Brothers E., Kudin K. N., Staroverov V. N., Kobayashi R., Normand J., Raghavachari K., Rendell A., Burant J. C., Iyengar S. S., Tomasi J., Cossi M., Rega N., Millam N. J., Klene M., Knox J. E., Cross J. B., Bakken V., Adamo C., Jaramillo J., Gomperts R., Stratmann R. E., Yazyev O., Austin A. J., Cammi R., Pomelli C., OchterskiJ W., Martin R. L., Morokuma K., Zakrzewski V. G., Voth G. A., Salvador P., Dannenberg J. J., Dapprich S., Daniels A. D., Farkas O., Foresman J. B., Ortiz J. V., Cioslowski J. and Fox D. J. (2009) *Gaussian09 Revision D.01*. GaussianInc, Wallingford, CT.

Fuller C. C., Davis J. A. and Waychunas G. A. (1993) Surface chemistry of ferrihydrite: part 2. Kinetics of arsenate adsorption and coprecipitation. *Geochim. Cosmochim. Acta* **57**, 2271–2282.

Glasby G. P. (2006) Manganese: predominant role of nodules and crusts. In *Marine Geochemistry* (eds. H. D. Schulz and M. Zabel). Springer, Berlin, pp. 371–427.

Gu C., Wang Z., Kubicki J. D., Wang X. and Zhu M. (2016) X-ray absorption spectroscopic quantification and speciation modeling of sulfate adsorption on ferrihydrite surfaces. *Environ. Sci. Technol.* **50**, 8067–8076.

Hay P. J. and Wadt W. R. (1985) Ab initio effective core potentials for molecular calculations. Potentials for the transition metal atoms Sc to Hg. *J. Chem. Phys.* **82**, 270–283.

Hein J. R., Koschinsky A. and Halliday A. N. (2003) Global occurrence of tellurium-rich ferromanganese crusts and a model for the enrichment of tellurium. *Geochim. Cosmochim. Acta* **67**, 1117–1127.

Hein J. R., Conrad T. A., Frank M., Christl M. and Sager W. W. (2012) Copper-nickel-rich, amalgamated ferromanganese crust-nodule deposits from Shatsky Rise, NW Pacific. *Geochem., Geophys., Geosyst.* **13**, Q10022.

Hein J. R., Mizell K., Koschinsky A. and Conrad T. A. (2013) Deep-ocean mineral deposits as a source of critical metals for high- and green-technology applications: Comparison with land-based resources. *Ore. Geol. Rev.* **51**, 1–14.

Jain A. and Loeppert R. H. (2000) Effect of competing anions on the adsorption of arsenate and arsenite by ferrihydrite. *J. Environ. Qual.* **29**, 1422–1430.

James R. O. and Healy T. W. (1972) Adsorption of hydrolyzable metal ions at the oxide-water interface III. A thermodynamic model of adsorption. *J. Colloid. Interf. Sci.* **40**, 65–81.

Kashiwabara T., Mitsunobu S., Das A., Itai T., Tanimizu M. and Takahashi Y. (2008) Oxidation states of antimony and arsenic in marine ferromanganese oxides related to their fractionation in oxic marine environment. *Chem. Lett.* **37**, 756–757.

Kashiwabara T., Takahashi Y., Tanimizu M. and Usui A. (2011) Molecular-scale mechanisms of distribution and isotopic fractionation of molybdenum between seawater and ferromanganese oxides. *Geochim. Cosmochim. Acta* **75**, 5762–5784.

Kashiwabara T., Takahashi Y., Marcus M. A., Uruga T., Tanida H., Terada Y. and Usui A. (2013) Tungsten species in natural ferromanganese oxides related to its different behavior from molybdenum in oxic ocean. *Geochim. Cosmochim. Acta* **106**, 364–378.

Kashiwabara T., Oishi Y., Sakaguchi A., Sugiyama T., Usui A. and Takahashi Y. (2014) Chemical processes for the extreme enrichment of tellurium into marine ferromanganese oxides. *Geochim. Cosmochim. Acta* **131**, 150–163.

Kitahama K., Kiriyama R. and Yoshida B. (1975) Refinement of the crystal structure of scorodite. *Acta. Crystallogr. Sect. B: Struct. Sci.* **B31**, 322–324.

Koschinsky A. and Halbach P. (1995) Sequential leaching of marine ferromanganese precipitates: Genetic implications. *Geochim. Cosmochim. Acta* **59**, 5113–5132.

Koschinsky A. and Hein J. R. (2003) Uptake of elements from seawater by ferromanganese crusts: solid-phase associations and seawater speciation. *Mar. Geol.* **198**, 331–351.

Langmuir D. (1997) *Aqueous environmental geochemistry*. Prentice Hall, Upple Saddle River.

Lee C. T., Yang W. T. and Parr R. G. (1988) Development of the Colle-Salvetti correlation energy formula into a functional of the electron density. *Phys. Rev. B* **37**, 785–789.

Li J., Wang X., Zhao G., Chen C., Chai Z., Alsaedi A., Hayat T. and Wang X. (2018) Metal-organic framework-based materials: superior adsorbents for the capture of toxic and radioactive metal ions. *Chem. Soc. Rev.* **47**, 2322–2356.

Li Y. H. (1982) Interelement relationship in abyssal Pacific ferromanganese nodules and associated pelagic sediments. *Geochim. Cosmochim. Acta* **46**, 1053–1060.

Liu H., Lu X., Li J., Chen X., Zhu X., Xiang W., Zhang R., Wang X., Lu J. and Wang R. (2017) Geochemical fates and unusual distribution of arsenic in natural ferromanganese duricrust. *Appl. Geochem.* **76**, 74–87.

Manceau A. (1995) The mechanism of anion adsorption on iron oxides: Evidence for the bonding of arsenate tetrahedra on free $Fe(O, OH)_6$ edges. *Geochim. Cosmochim. Acta* **59**, 3647–3653.

Manceau A., Lanson B. and Drits V. A. (2002) Structure of heavy metal sorbed birnessite. Part III. Results from powder and polarized extended X-ray absorption fine structure spectroscopy. *Geochim. Cosmochim. Acta* **66**, 2639–2663.

Manceau A., Lanson M. and Geoffroy N. (2007) Natural speciation of Ni, Zn, Ba, and As in ferromanganese coatings on quartz using X-ray fluorescence, absorption, and diffraction. *Geochim. Cosmochim. Acta* **71**, 95–128.

Manceau A., Tamura N., Celestre R. S., Macdowell A. A., Geoffroy N., Sposito G. and Padmore H. A. (2003) Molecularscale speciation of Zn and Ni in soil ferromanganese nodules from loess soils of the Mississippi Basin. *Environ. Sci. Technol.* **37**, 75–80.

Mandal B. K. and Suzuki K. T. (2002) Arsenic round the world: A review. *Talanta* **58**, 201–235.

Marcus M. A., Manceau A. and Kersten M. (2004) Mn, Fe, Zn and As speciation in a fast-growing ferromanganese marine nodule. *Geochim. Cosmochim. Acta* **68**, 3125–3136.

Marcus M. A., Edwards K. J., Gueguen B., Fakra S. C., Horn G., Jelinski N. A., Rouxel O., Sorensen J. and Toner B. M. (2015) Iron mineral structure, reactivity, and isotopic composition in a South Pacific Gyre ferromanganese nodule over 4 Ma. *Geochim. Cosmochim. Acta* **171**, 61–79.

Miertus S., Scrocco E. and Tomasi J. (1981) Electrostatic interaction of a solute with a continuum. A direct utilization of *ab initio* molecular potentials for the prevision of solvent effects. *Chem. Phys.* **55**, 117–129.

Mitsunobu S., Harada T. and Takahashi Y. (2006) Comparison of antimony behavior with that arsenic under various soil redox conditions. *Environ. Sci. Technol.* **40**, 7270–7276.

Mitsunobu S., Takahashi Y., Terada Y. and Sakata M. (2010) Antimony (V) incorporation into synthetic ferrihydrite, goethite, and natural iron oxyhydroxides. *Environ. Sci. Technol.* **44**, 3712–3718.

Murray J. W. and Dillard J. G. (1979) The oxidation of cobalt(II) adsorbed on manganese dioxide. *Geochim. Cosmochim. Acta* **43**, 781–787.

Ona-Nguema G., Morin G., Juillot F., Calas G. and Brown G. E. (2005) EXAFS analysis of arsenite adsorption onto two-line ferrihydrite, hematite, goethite, and lepidocrocite. *Environ. Sci. Technol.* **39**, 9147–9155.

Qin H. B., Yokoyama Y., Fan Q., Iwatani H., Tanaka K., Sakaguchi A., Kanai Y., Zhu J. M., Onda Y. and Takahashi Y. (2012) Investigation of cesium adsorption on soil and sediment samples from Fukushima Prefecture by sequential extraction and EXAFS technique. *Geochem. J.* **46**, 297–302.

Qin H. B., Zhu J. M., Liang L., Wang M. S. and Su H. (2013) The bioavailability of selenium and risk assessment for human selenium poisoning in high-Se areas. *China. Environ. Int.* **52**, 66–74.

Qin H. B., Takeichi Y., Nitani H., Terada Y., Harada T. and Takahashi Y. (2017a) Tellurium distribution and speciation in contaminated soils from abandoned mine tailings: Comparison with selenium. *Environ. Sci. Technol.* **51**, 6027–6035.

Qin H. B., Zhu J. M., Lin Z. Q., Xu W. P., Tan D. C., Zheng L. R. and Takahashi Y. (2017b) Selenium speciation in seleniferous agricultural soils under different cropping systems using sequential extraction and X-ray absorption spectroscopy. *Environ. Pollut.* **225**, 361–369.

Ravel B. and Newville M. (2005) ATHENA, ARTEMIS, HEPHAESTUS: data analysis for X-ray absorption spectroscopy using IFEFFIT. *J. Synchrotron. Radiat.* **12**, 537–541.

Reimers J. N., Greedan J. E. and Subramanian M. A. (1989) Crystal structure and magnetism in $MnSb_2O_6$: Incommensurate long-range order. *J. Solid. State. Chem.* **79**, 263–276.

Scheinost A. C., Rossberg A., Vantelon D., Xifra I., Kretzschmar R., Leuz A. K., Funke H. and Johnson C. A. (2006) Quantitative antimony speciation in shooting-range soils by EXAFS spectroscopy. *Geochim. Cosmochim. Acta* **70**, 3299–3312.

Schwertmann U. and Cornell R. M. (2000) *Iron Oxides in the Laboratory*, second ed. Wiley-VCH, p. 103pp.

Sherman D. M. and Randall S. R. (2003) Surface complexation of arsenic(V) to iron(III) (hydr)oxides: Structural mechanism from ab initio molecular geometries and EXAFS spectroscopy. *Geochim. Cosmochim. Acta* **22**, 4223–4230.

Stephens P. J., Devlin F. J., Chabalowski C. F. and Frisch M. J. (1994) Ab initio calculation of vibrational absorption and circular dichroism spectra using density functional force fields. *J. Phys. Chem.* **98**, 11623–11627.

Tanaka M., Togo Y. S., Yamaguchi N. and Takahashi Y. (2014) An EXAFS study on the adsorption structure of phenyl-substituted organoarsenic compounds on ferrihydrite. *J. Colloid. Interface. Sci.* **415**, 13–17.

Tanaka M., Ariga D., Kashiwabara T. and Takahashi Y. (2018) Adsorption mechanism of molybdenum(vi) on manganese oxides causing a large isotope fractionation. *ACS Earth. Space. Chem.* **2**, 1187–1195.

Takahashi Y., Manceau A., Geoffroy N., Marcus M. A. and Usui A. (2007) Chemical and structural control of the partitioning of Co, Ce, and Pb in marine ferromanganese oxides. *Geochim. Cosmochim. Acta* **71**, 984–1008.

Takahashi Y., Ariga D., Fan Q. and Kashiwabara T. (2015) Systematics of distributions of various elements between ferromanganese oxides and seawater from natural observation, thermodynamics, and structures. In *Subseafloor Biosphere Linked to Hydrothermal Systems: TAIGA Concept*. Springer, pp. 39–48.

Tokunaga K. and Takahashi Y. (2017) Effective removal of selenite and selenate ions from aqueous solution by barite. *Environ. Sci. Technol.* **51**, 9194–9201.

Tokoro C., Yatsugi Y., Koga H. and Owada S. (2010) Sorption mechanisms of arsenate during coprecipitation with ferrihydrite in aqueous solution. *Environ. Sci. Technol.* **44**, 638–643.

Violante A., Gaudio S. D., Pigna M., Ricciardella M. and Banerjee D. (2007) Coprecipitation of arsenate with metal oxides. 2. nature, mineralogy, and reactivity of iron(III) precipitates. *Environ. Sci. Technol.* **41**, 8275–8280.

U.S. Geological Survey, 2012, Mineral commodity summaries 2012: U.S. Geological Survey, Washington D.C.

Usui Akir and Someya Masa (1997) *Distribution and composition of marine hydrogenetic and hydrothermal manganese deposits in the northwest Pacific*. Geological Society Special Publication No. 119, London, pp. 177–198.

Villalobos M., Toner B., Bargar J. and Sposito G. (2003) Characterization of the manganese oxide produced by *Pseudomonas putida strain MnB1*. *Geochim. Cosmochim. Acta* **67**, 2649–2662.

Villalobos M., Escobar-Quiroz I. N. and Salazar-Camacho C. (2014) The influence of particle size and structure on the sorption and oxidation behavior of birnessite: I. Adsorption of As(V) and oxidation of As(III). *Geochim. Cosmochim. Acta* **125**, 564–581.

Wadt W. R. and Hay P. J. (1985) Ab initio effective core potentials for molecular calculations. Potentials for main group elements Na to Bi. *J. Chem. Phys.* **82**, 284–298.

Waychunas G. A., Rea B. A., Fuller C. C. and Davis J. A. (1993) Surface-chemistry of ferrihydrite: Part 1. EXAFS studies of the geometry of coprecipitated and adsorbed arsenate. *Geochim. Cosmochim. Acta* **57**, 2251–2269.

Wilkie J. A. and Hering J. G. (1996) Adsorption of arsenic onto hydrous ferric oxide: effects of adsorbate/adsorbent ratios and co-occurring solutes. *Colloid. Surf. A.* **107**, 97–110.

Wu Z., He M., Guo X. and Zhou R. (2010) Removal of antimony (III) and antimony (V) from drinking water by ferric chloride coagulation: Competing ion effect and the mechanism analysis. *Sep. Purif. Technol* **76**, 184–190.

Ying S. C., Kocar B. D. and Fendorf S. (2012) Oxidation and competitive retention of arsenic between iron- and manganese oxides. *Geochim. Cosmochim. Acta* **96**, 294–303.

Yang S., Uesugi S., Qin H. B., Tanaka M., Kurisu M., Miyamoto C., Kashiwabara T., Usui A. and Takahashi Y. (2019) Comparison of arsenate and molybdate speciation in hydrogenetic ferromanganese Nodules. *ACS Earth Space Chem.* **3**, 29–38.

Zabinsky S. I., Rehr J. J., Ankudinov A., Albers R. C. and Eller M. J. (1995) Multiple-scattering calculations of X-ray-absorption spectra. *Phys. Rev. B* **52**, 2995–3009.

Zhang G., Liu F., Liu H., Qu J. and Liu R. (2014) Respective role of Fe and Mn oxide contents for arsenic sorption in iron and manganese binary oxide: An X-ray absorption spectroscopy investigation. *Environ. Sci. Technol.* **48**, 10316–10322.

Associate editor: Mario Villalobos